

Article

Relative Azimuthal-Angle Matching (RAM): A Screening Method for GEO-LEO Reflectance Comparison in Middle Latitude Forests

Yusuke Adachi , Ryota Kikuchi, Kenta Obata  and Hiroki Yoshioka * 

Department of Information Science and Technology, Aichi Prefectural University, 1522-3 Ibaragabasama, Nagakute, Aichi 480-1198, Japan; id181001@cis.aichi-pu.ac.jp (Y.A.); is141028@cis.aichi-pu.ac.jp (R.K.); obata@ist.aichi-pu.ac.jp (K.O.)

* Correspondence: yoshioka@ist.aichi-pu.ac.jp; Tel.: +81-561-76-8774

Received: 18 March 2019; Accepted: 23 April 2019; Published: 8 May 2019



Abstract: This study introduced a data screening method for comparing the reflectances in middle latitude forest regions collected by a Geostationary Earth Observing (GEO) satellite and a Low Earth Orbit (LEO) satellite. This method attempts to reduce the differences between the relative azimuth angles of the GEO and LEO observations. The method, called relative azimuthal-angle matching (RAM), takes advantage of the high temporal resolution of the GEO satellites, which enables collection of a wide range of relative azimuth angles within a day. The performance of the RAM method was evaluated using data in the visible and near-infrared bands collected by the Himawari-8/Advanced Himawari Imager (AHI) and the Terra/Moderate Resolution Imaging Spectroradiometer (MODIS). The consistency of the reflectance pairs of MODIS and AHI selected by the RAM method was compared with the consistency of the reflectance pairs acquired simultaneously by the two sensors. The data were matched pixel-by-pixel after applying atmospheric corrections and cloud screening. The results show that RAM improved the reflectance ratio by approximately 10% for the red and NIR bands on average relative to the simultaneous observations. Significant improvements in the two bands were observed (20%), especially among data collected in the fall and winter. Performance of RAM depends largely on season. Especially in summer, the reflectance pair chosen by RAM showed less consistency than solar zenith-angle matching (SZM). The results also indicated the relatively large influence of the spectral response functions on the green and red bands of the two sensors.

Keywords: GEO; LEO; screening; Himawari-8; AHI; Terra; MODIS

1. Introduction

Geostationary earth observing (GEO) satellites have played a major role in various fields of study for decades. The primary focus of their contribution historically has been in the atmospheric and oceanic sciences. In recent years, much attention has been paid to the applications of GEO satellite to land observation [1–5] because of the enhanced band configuration and calibration strategy [4,6,7]. These “new generation” GEO satellites, such as the Himawari-8 (2014–) [6], FY-4A [4], and GOES-16 (2016–) [7], have land monitoring capabilities with high radiometric and temporal resolutions, in addition to their primary atmosphere and ocean sciences monitoring capabilities. The enhanced capabilities will bring new observation opportunities, especially in land applications in which satellite data having such a high temporal resolution do not currently exist.

Limiting our discussion to land monitoring applications [8–14], the use of GEO satellite data will require us to address issues of data consistency between the established LEO satellite data and the GEO satellite data. A consistency analysis is expected to be conducted prior to any data analysis

applications in this context. Yeom et al. [14] used the normalized difference vegetation index (NDVI) derived from a GEO satellite to estimate paddy productivities in a middle latitude region. In their work, the first step in the data consistency analysis involved comparing the GEO-based NDVI profiles with the LEO-based NDVI. Data consistency analysis is complex and particularly difficult when comparing middle latitude regions because standard techniques, such as ray-matching methods [15,16], cannot be applied due to differences in the sun-target-sensor geometries of the GEO and LEO observations. Data observations collected from targets in the middle latitude by the GEO and LEO satellites will not be collected under identical geometries. The geometric differences induce bidirectional effects on the observed land surface, causing fluctuations in the observed reflectances. These fundamental issues must be addressed to improve our understanding of the data collected from GEO satellites.

Considerable effort has been directed toward comparing and inter-calibrating data collected from multiple LEO satellites. A comprehensive review of reflectance data was assembled by Chander et al. [17]. Systematic comparative studies on the spectral vegetation index (VI) have also been conducted by many researchers, as reported recently by Fan and Liu [18]. Comparison techniques and protocols as well as state-of-the-art inter-calibration standards have been established. One remarkable technique is the ray-matching method [15,16]. This method imposes tight screening criteria to ensure the selection of identical sun-target-sensor geometries among sensor pairs. The method has been widely used and successfully applied in the context of the inter-calibration of LEO-LEO radiances and reflectances [19] and VI products [20]. Another technique is the simultaneous nadir overpass (SNO) technique, introduced by Heidinger et al. [21] and Cao et al. [22]. The technique has been applied successfully to LEO-LEO inter-calibration problems [23,24].

Unlike the LEO-LEO comparisons, comparisons between GEO and LEO satellites [25–27] are complicated by the fact that LEO and GEO data are seldom acquired under identical viewing and illumination conditions. This “conditional mismatch” is especially prominent in regions located at middle to high latitudes. For example, the relative azimuth angles of the GEO and LEO satellite sensors examined in this study differed by between 3° and 41° under simultaneous observation conditions in middle latitudes. This fact suggests that GEO and LEO satellite data comparisons at middle to high latitudes might suffer from unavoidable biases caused by conditional mismatches. Although these differences can be rectified by developing a site-specific bidirectional reflectance distribution function (BRDF) to describe well-characterized targets [27,28], this is not always possible for complex surfaces, such as mountainous forests.

This study is not intended to discuss GEO and LEO satellite inter-calibration techniques; the ray-matching condition, for instance, is difficult to satisfy for a target located in middle to high latitudes. Our intention is straightforward: We addressed the issue of unavoidable differences that a user may encounter when attempting to compare data from sensors in GEO and LEO satellites over a region of interest (ROI) located at middle latitudes [29]. Furthermore, we developed a screening criterion specific for GEO-LEO comparisons that provides an alternative to simultaneous observation conditions at locations not amenable to sophisticated ray-matching methods. We proposed to identify GEO and LEO data pairs having identical magnitude solar-to-sensor relative azimuth angles. This screening criterion may be met by sacrificing the condition of simultaneous observation. The proposed criterion has both advantages and disadvantages compared to the simultaneous observation criterion. We demonstrated this approach using the Himawari-8/Advanced Himawari Imager (AHI) and Terra/Moderate Resolution Imaging Spectroradiometer (MODIS) as representative GEO-LEO data pairs.

Herein, we first describe our data screening method for comparing GEO-LEO reflectance data in middle latitude regions (Section 2). Data descriptions (Section 3) and algorithm details (Section 4) follow the Method Section. The comparison results are presented in Section 5 and discussed in Section 6. Finally, this work is concluded in Section 7.

2. Method

GEO-LEO reflectance comparisons in a middle latitude are illustrated in Figure 1. The right polar plot in Figure 1 shows the angular positions of the MODIS and AHI satellites in one of our ROIs, a forest in Kochi, Japan. In the polar plot, blue circles (filled or empty) represent combinations of the view zenith and view azimuth angles in the MODIS data, which cover all sixteen observations within a single revisit cycle (from 11 May 2016 to 26 May 2016) of the Terra satellite. The view zenith angle of the MODIS data varies from 0° (nadir) to 60° . The angular position of the AHI observations, depicted by the red filled circle, remains fixed at one location due to its geostationary orbit. The polar plot indicates the fact that the two sensors never observe this ROI from the same direction. The geometrical mismatch between the GEO and LEO satellites makes reflectance comparisons difficult, especially for targets with an unknown directional dependency (often modeled using the BRDF). For example, the left figure in Figure 1 shows a scatter plot of the MODIS band-4 reflectance observations acquired over three consecutive days versus the reflectances of the AHI band-2 simultaneous observations over the ROI. The figure shows systematic differences, suggesting that the angular mismatch caused significant biases, even though we selected simultaneous observations as a screening criterion in the GEO and LEO satellites reflectance comparisons over a middle latitude forest region.

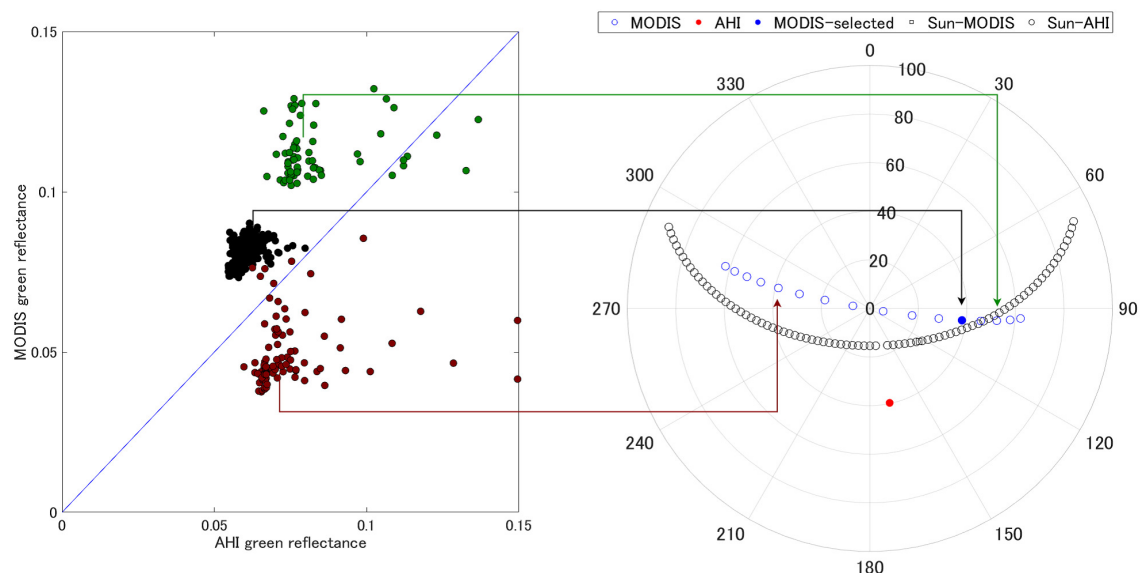


Figure 1. Scatter plot (left) of the TOC reflectances observed by AHI and MODIS, with the corresponding green bands. The data were extracted from our test site over the Kochi Forest during the period between 12 and 14 May 2016. The observation pairs over the three days are indicated by different colors. The data acquisition times of the three groups of reflectance pairs were nearly identical. (right) A polar plot of the illumination and view angles. Sixteen variations in the MODIS view angles (11–26 May 2016) are also plotted.

Again, in contrast to the MODIS observations, AHI observes the same target always from a fixed direction, resulting in fixed view zenith and view azimuth angles for the target. This fact is indicated by the red filled circle in the polar plot shown in Figure 1. The view zenith and azimuth angles of AHI for this specific target were 40° and 168° , respectively. Although there is no freedom of choice regarding the view angles of AHI, the advantage of AHI is its high temporal resolution (10 min for the full-disk observation mode). Because of this advantage, the illumination direction (pairs of solar zenith and solar azimuth angles) varies significantly from sunrise to sunset, as indicated by the empty black circles in the polar plot shown in Figure 1. This temporal high resolution brings a variety of choices in both the solar zenith and relative azimuth angles for the AHI observations. The wide range of angular variations suggests the possibility of a better screening criterion than the criterion of simultaneous

observation in the context of GEO-LEO reflectance comparisons at middle latitudes. One candidate screening criterion is the selection of AHI observations based on the relative azimuth angle: We always have a choice of AHI observation with relative azimuth angles that are nearly identical to those of the MODIS observations. This criterion is referred to here as relative azimuthal-angle matching (RAM). The selection of simultaneous AHI and MODIS observations is standard practice. Simultaneous observations yield the same solar zenith angle (and different relative azimuth angle); therefore, we denote this criterion the solar zenith-angle matching (SZM) criterion in this study.

Differences between the RAM and SZM methods are summarized in Table 1 by focusing on the angular conditions satisfied and the differences in the atmospheric conditions. During the initial data screening process for AHI-MODIS comparisons, we can select MODIS observations with a view zenith angle closest to that of the AHI data (e.g., an angle of 40° , depicted by filled blue circles in the polar plot shown in Figure 1). Once this choice is made based on the MODIS view-zenith angle, one has at least two screening criteria: (a) SZM (choice of AHI data with the solar zenith angle closest to that of the MODIS observation); and (b) RAM (choice of AHI data with the relative azimuth angle closest to that of the MODIS observation). Figure 2a shows the angular position of the sun and sensors for an AHI scene selected using the SZM method. The idea of using simultaneous/near-simultaneous observations has been used in other intercalibration studies. The directions of the sun relative to the two sensors are not, in general, identical (clockwise or counter-clockwise) for an ROI, and the relative azimuth angles between the sensor and the sun are not identical in the AHI and MODIS observations. Figure 2b shows an example of the RAM method. This method sacrifices consistency in observation time rather than sacrificing consistency in the relative azimuth angle. Again, it should be noted that the SZM method involves the choice of nearly simultaneous observations of AHI with MODIS. The SZM method guarantees identical atmospheric conditions for the GEO and LEO observations, whereas RAM does not (due to differences in the observation times). In the RAM method, the two sensors observe a target from different view azimuth angles, although the relative azimuth angle is nearly identical. In other words, RAM assumes that surface scattering is rotationally symmetric in the azimuthal direction. Thus, the performance of the RAM method depends on the level of rotational symmetry. Despite differences in the atmospheric conditions for the two observations and the assumption of rotational symmetry, our hypothesis is that for targets located at middle latitudes, SZM would not always be the better pair selection method compared to RAM in the context of GEO-LEO reflectance comparisons. This study investigated this point to improve our understanding of GEO-LEO inter-comparisons at middle latitudes.

Table 1. Differences in the geometric and atmospheric conditions of the LEO and GEO observation pairs selected using the SZM and RAM methods. The mark “o” indicates that the GEO and LEO observation conditions are nearly identical. The numbers indicate the ranges of absolute differences in this study. The SZM method corresponds to simultaneous data acquisition; therefore, the atmospheric conditions will be identical.

Method	Solar Zenith	View Zenith	View Azimuth	Relative Azimuth	Atmospheric Condition
SZM	o	o	$\sim 70^\circ$	0° to 50°	o
RAM	0° to 20°	o	same as SZM	o	1.5 to 5.5 h

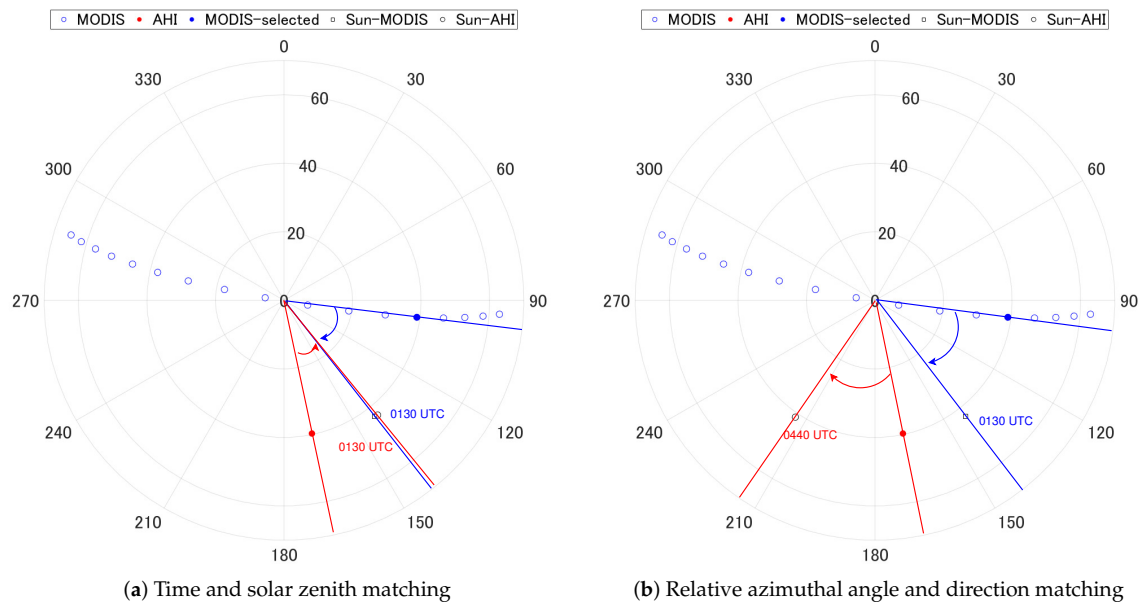


Figure 2. Angular conditions of the sun, MODIS, and AHI for the SZM method (a) and RAM method (b) over the ROI of the Kochi Forest. The observation data for this plot span the period between 1 and 16 March (16 days) 2018. The time difference is minimal in (a) but the relative azimuth angles are not identical. The relative azimuth angles are almost identical in (b), but the time difference is large.

3. Data Description

To meet our objectives, we set several conditions to be satisfied by selected test sites. The first condition is the location of the sites. Because the ray-matching method condition in the context of GEO-LEO comparisons is generally limited to 20° north or south of the equator, targets of this study should be located outside of the latitude range. We set the condition to be even more stringent; the target must be located in a middle latitude region, preferably beyond 30° north or south of the equator. By setting this restriction, the geometric requirements of the ray-matching method are not satisfied. The meridian of the Himawari-8, 140.7° E, was used as the reference meridian of each test site. The second condition applied to the surface type. Forest targets, our primary interest, should be moderately uniform and homogeneous. Moreover, the terrain of the forest targets is preferably mountainous rather than a flat surface, which would make the conditions more difficult to satisfy using the RAM method. In addition to the forest targets, we must also select a test site corresponding to a non-vegetated surface as a reference location near the forest targets. By comparing the results of the mountainous forest with those obtained from non-vegetated flat targets, the influence of the vegetation quantity on the GEO-LEO comparison can be evaluated. These considerations and restrictions led us to select two pairs of forested and urban sites from the northern hemisphere, as described below.

3.1. Test Site

Four regions of interest (ROIs) located in Japan were used as our test sites (Figure 3). The ROIs include two forest sites: one from Kochi Prefecture on Shikoku Island and one from Aichi Prefecture on Honshu Island. Both ROIs were 20 km by 20 km. The ROIs of the non-vegetation targets were chosen from urban areas near the forest sites. The urban site near the Kochi Forest was 3 km by 5 km, and that near the Aichi Forest was 10 km by 10 km, as summarized in Table 2. The locations of these ROIs are shown on the map of the MODIS leaf area index (LAI) in Figure 3. The data obtained from MOD15A2H [30] on 17 May 2017 were used to verify the LAI over the ROIs.

The LAIs and its spatiotemporal variations were analyzed over the two forest sites. The daily LAI data from MOD15A2H were used by focusing on a one-year period in 2017. We used the data

that passed all the quality control examination based on the FparLai_QC flags. Especially in this analysis, the flag was also used to identify pixels with a LAI value retrieved using the radiative transfer (RT) model algorithm. The yearly average and standard deviation at each site was computed using the daily data only if more than 25% of all pixels passed the cloud and FparLai_QC flag screening criteria. After screening, we computed the spatially and temporally averaged LAI over the year 2017 over the two forest ROIs. The average LAIs over the Kochi and Aichi Forests were both 2.3, and the corresponding standard deviations were 0.38 and 0.46, respectively. These results revealed small variations in the LAIs over these ROIs. This trend was confirmed from the High-Resolution Land Use and Land Cover (HRLULC) map data (30 m grid) distributed by JAXA [31]. The land cover map indicated that the proportions of evergreen needle-leaved forest (ENF) and evergreen broad-leaved forest (EBF) in the Kochi Forest were 66.5% and 25.7%, respectively. In the Aichi Forest, the proportions were 83.9% and 4.4%, respectively. Therefore, the two ROIs were mostly composed of ENF and EBF, yielding spatially homogeneous and temporally stable LAIs over the ROIs.

Table 2. Latitude and longitude ranges of the ROIs.

ROI	Range (Latitude/Longitude)
Forest in Kochi (KochiForest)	33.485–33.675° N / 133.985–134.175° E
Forest in Aichi (AichiForest)	34.995–35.185° N / 137.285–137.475° E
Urban in Kochi (KochiUrban)	33.555–33.575° N / 133.525–133.565° E
Urban in Aichi (AichiUrban)	35.095–35.185° N / 136.855–136.945° E

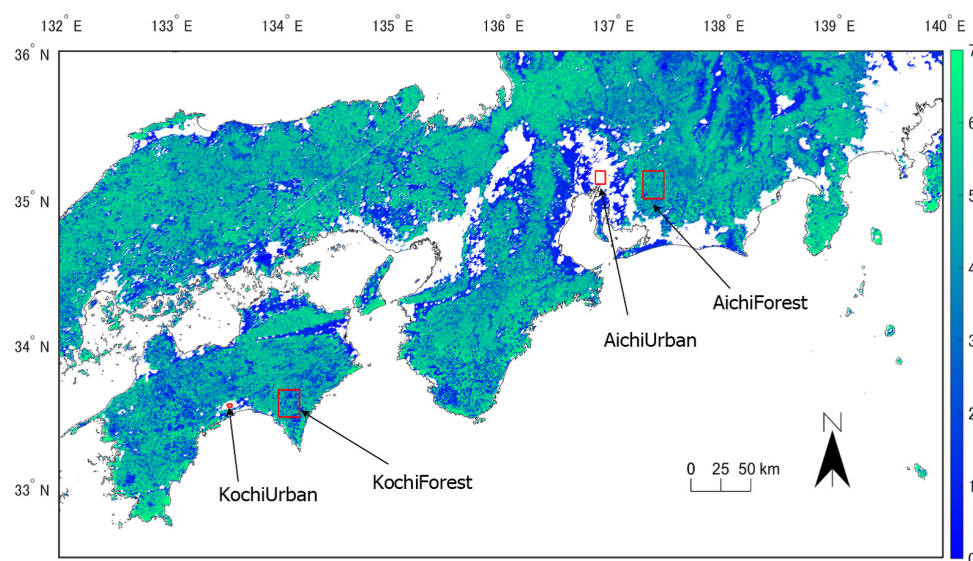


Figure 3. Spatial distribution of the LAI in the western part of Japan, based on the MOD15A2H data collected on 17 May 2017. Four ROIs are indicted by rectangles. LAI values of the non-vegetated regions, such as the urban and ocean regions, are represented by the white background.

3.2. Satellite Data

Himawari-8 is located at 140.7° E longitude and observes regions in East Asia and the Western Pacific. The standard data providing “Full Disk” coverage were downloaded from the National Institute of Information and Communications Technology (NICT) Science Cloud. The temporal resolution of the Full Disk observation is 10 min. We compared four visible and near-infrared bands (band 1–4) of the AHI with the corresponding MODIS bands in this study. The central wavelengths of the four AHI bands were 460 nm, 510 nm, 640 nm, and 860 nm. The spatial resolution was 1 km at the sub-satellite point, except in band 3. The resolution of band 3 was 0.5 km [6]. The data from

band-3 were averaged over 2 by 2 pixel blocks to match the resolution of the other bands. The scaled digital counts (called the calibrated reflectances) were then transformed into the actual reflectance by considering the solar zenith angle and the square of the sun-earth distance using the calibration coefficients provided.

The Terra satellite is in LEO with a morning overpass time and 16-day revisit cycle. We used the MODIS Calibrated Radiances, the Daily L1B Swath 1 km (MOD021KM) Collection 6 [32] and MODIS Geolocation Fields Daily L1A Swath 1 km (MOD03) Collection 6 [33], downloaded from the Level-1 and Atmosphere Archive and Distribution System (LAADS) Distributed Active Archive Center (DAAC). Bands 3, 4, 1, and 2 of the MODIS data corresponded to bands 1–4 of the AHI data, respectively. The central wavelengths of the MODIS bands were 465.7 nm, 553.7 nm, 646.3 nm, and 856.5 nm, respectively [34]. The digital counts were also transformed into actual reflectances in the same manner as was used with the AHI data [35]. The MODIS cloud mask data (MOD35) Collection 6.1 [36] was also used for screening purposes.

In this work, the data acquisition times for both the AHI and MODIS data were represented by four digits, “HHMM”, derived from the time stamp included in the file name, where “HH” and “MM” stand for the hour and minute of the day, respectively. The time stamp in the file name indicated the beginning of the scan for a full AHI disk and the 5-min MODIS granule. Note that the true observation time for each location was slightly different (1–5 min) from this abbreviated information.

4. Algorithm

The AHI and MODIS reflectances were compared using the algorithm illustrated in Figure 4. The figure provides an overview of the data processing flow in this study. The entire process was divided into two parts: (a) geometric condition retrieval; and (b) preprocessing and screening (see Figure 4). Part (a) involved identifying pairs of data acquisition times in the MODIS and AHI observations that satisfied the SZM or RAM criteria. The process began with the selection of the MODIS scenes based on a view zenith angle criterion (Section 4.1). After this selection, data from the same orbital path were collected so that only MODIS data having a view zenith angle identical to that of the AHI data were prepared for processing. The outputs from this process were the time of day for the SZM and RAM data that satisfied the geometric conditions of these screening methods. Part (b) of the flowchart mainly performed preprocessing and screening, such as data preparation and compositing for AHI (Section 4.2), atmospheric corrections (Section 4.3), and cloud screening (Section 4.4). After the second analysis step, two pairs of MODIS and AHI reflectances were obtained at each pixel (1 km resolution) and in each band; one pair corresponded to the SZM method and the other to the RAM method (Section 4.5). Finally, the reflectance ratios between the two sensors were computed (Section 4.6). These processes are explained in detail below.

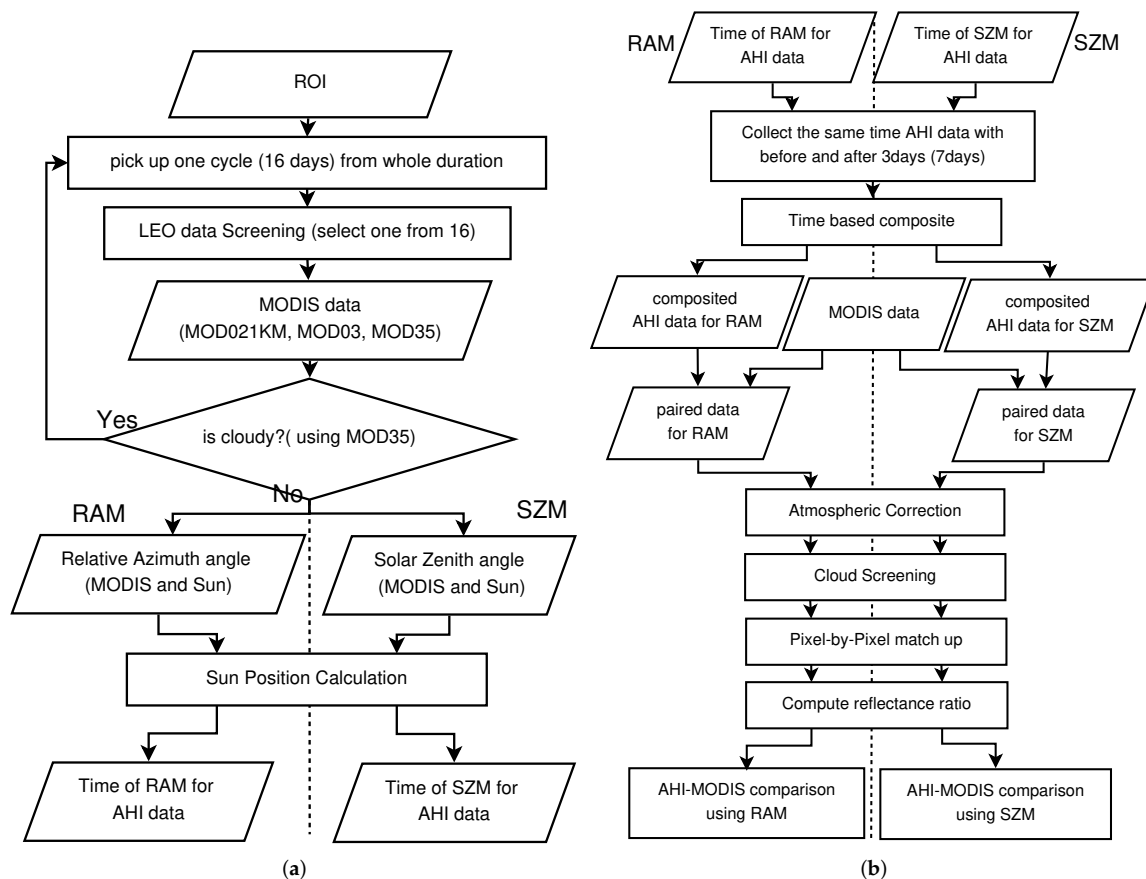


Figure 4. Flow chart describing the algorithm used for GEO-LEO reflectance comparisons (AHI and MODIS); (a) geometric condition retrieval; and (b) preprocessing, screening, and subsequent processing for comparison.

4.1. MODIS Scene Selection Based on the AHI View Zenith Angle

Our algorithm began by focusing on a single revisit cycle of Terra. During the duration of one revisit cycle, MODIS observes an ROI from 16 different orbital paths, resulting in 16 different combinations of view zenith and view azimuth angles for a given ROI. Among these observations (MOD02), the view zenith angle varied from 0° to nearly 60° , as shown in Figure 1. This wide range of variation in the view zenith angle enabled us to select the angle closest to the AHI view zenith angle. Two choices are available: the west-looking observation and the east-looking observation. Among these two choices, the choice of the west-looking observations may be advantageous relative to the other for targets in the northern hemisphere. This constraint arises from the condition applied using the RAM method. In the RAM method, it is necessary to select an AHI observation having a relative azimuth angle that is nearly identical to that of the MODIS observation. West-looking observations result in smaller relative azimuth angles than the east-looking observations. It enables the RAM method to use data observed at relatively earlier time of the afternoon, which increases observation chances especially in winter before sunset. Note that the selection of the MODIS view zenith angle is common to both the SZM and RAM methods. Thus, our first step was to identify the MOD02 scene (out of 16 observations) having the view zenith angle closest to that of the AHI observation from among the west-looking observations.

The Himawari-8 is a geostationary satellite; therefore, view zenith and view azimuth angles of AHI are fixed for each target. These fixed angles can vary depending on the ROI location. Each ROI requires retrieval of the view zenith and view azimuth angles of the AHI observation prior to selecting the MODIS data. In summary, MODIS data selection was carried out in the following order: (1) AHI

view zenith angle for the ROI; and (2) selection of the MODIS data from among the 16-day observations with a view zenith angle closest to the AHI view zenith angle. This process was repeated every 16 days from 7 July 2015 to 31 August 2018 (three years). After applying these processes, we identified and selected one MOD02 for each 16-day window.

The next step was to filter out the MODIS data, pixel by pixel, based on the quality assurance (QA) flags of the MOD35 data. The “unobstructed FOV QA Flag” could be used to identify “confident clear” pixels. The pixels deemed “confident clear” were counted for all selected MODIS data over the three years (7 July 2015 to 31 August 2018). By focusing on a single month, three years of scenes were analyzed. We further selected the best monthly scenes from the three-year collections. The best scene was determined based on the number of pixels remaining after screening based on the QA flags. Finally, we selected one MODIS scene for each month, regardless of the year. Table 3 summarizes the best MODIS scene and the number of pixels remaining after the screening process had sorted pixels by day of the year (DOY), regardless of the year difference.

Table 3. Selected dates for the top MODIS data evaluated by the number of confident clear pixels over each ROI. Dates are represented by six characters, “YYMMDD” (Y, M, and D represent the year, month, and day, respectively). The number in parentheses is the day of the year. The third, fifth, seventh, and ninth columns show the number of pixels found to be confident clear in each ROI.

	KochiForest		AichiForest		KochiUrban		AichiUrban	
January	180126 (26)	196	170125 (25)	207	180110 (10)	1	170125 (25)	8
February	170224 (55)	217	160208 (39)	215	170224 (55)	1	160208 (39)	12
March	160325 (85)	232	160327 (87)	210	170328 (87)	4	160311 (71)	7
April	170413 (103)	225	180402 (92)	64	170429 (119)	4	160412 (103)	2
May	160512 (133)	237	180520 (140)	37	160512 (133)	4	180520 (140)	7
June	180603 (154)	125	170602 (153)	8	-	-	170602 (153)	13
July	160731 (213)	126	150731 (212)	216	-	-	180723 (204)	39
August	180806 (218)	121	180808 (220)	237	180806 (218)	3	180808 (220)	39
September	160901 (245)	231	160903 (247)	217	160901 (245)	3	160903 (247)	2
October	151017 (290)	229	151003 (276)	187	151017 (290)	2	151019 (292)	7
November	171107 (311)	219	171109 (313)	238	171107 (311)	5	171125 (329)	25
December	171209 (343)	246	151222 (356)	231	171209 (343)	4	161208 (343)	27

As outputs of this stage, we retrieved two different times of the day: the MODIS data acquisition time, which was used to select AHI data in the SZM method, and the time of the AHI observation that yielded the same relative azimuth angle as the MODIS observation. The latter time could be retrieved by simulating the dynamics of the solar position over the observation day for each ROI. We summarized the outputs (times for the SZM and RAM methods) along with the DOY selected in this study (Table 4). Note that the DOY shown in the table corresponds to the selected MODIS data summarized in Table 3. The time for SZM remained relatively fixed in each ROI at around 01:30 UTC (10:30 in local time) throughout the year. On the other hand, the time for RAM varied by both the geolocation and the DOY, ranging from 03:00 UTC (12:00 in local time) to 06:50 (15:50). The time data were used as inputs for the next part of the analysis, Part (b), as shown in the flowchart (Figure 4).

Table 4. UTC time and DOY for the selected AHI data in the SZM and RAM methods.

	January	February	March	April	May	June	July	August	September	October	November	December
DOY: KochiForest	26	55	85	103	133	154	213	218	245	290	311	343
time (SZM)	0130	0130	0130	0130	0130	0135	0130	0135	0130	0130	0130	0130
time (RAM)	0550	0510	0420	0350	0320	0310	0320	0330	0350	0510	0550	0620
DOY: AichiForest	25	39	87	92	140	153	212	220	247	276	313	356
time (SZM)	0120	0120	0120	0120	0120	0120	0120	0120	0120	0120	0120	0120
time (RAM)	0620	0550	0430	0420	0310	0300	0320	0330	0400	0500	0620	0650
DOY: KochiUrban	10	55	87	119	133	-	-	218	245	290	311	343
time (SZM)	0130	0130	0130	0130	0130	-	-	0135	0130	0130	0130	0130
time (RAM)	0610	0510	0410	0330	0320	-	-	0330	0350	0510	0550	0620
DOY: AichiUrban	25	39	71	103	140	153	204	220	247	292	329	343
time (SZM)	0120	0120	0120	0120	0120	0120	0120	0120	0120	0120	0120	0120
time (RAM)	0610	0550	0450	0400	0310	0300	0320	0330	0400	0530	0640	0650

4.2. AHI Data Selection and Weekly Composites for the SZM and RAM Methods

The first step of Part (b) involved selecting AHI candidate data for comparison. We combined AHI data over one week periods for each MODIS observation to span three days before and after the MODIS observation. Although AHI observed the ROIs every 10 min, not all data were used. The data were screened based on the time information retrieved at the end of the previous analysis section, Part (a). We only used AHI data having an observation time close to either the SZM or RAM on each day. At this stage, we selected seven AHI scenes in the SZM and RAM methods, for a total of 14 scenes at each ROI.

These data were then composited to produce two datasets by targeting a specific time of observation. One set was for the SZM method and the other was used for the RAM method. For this selection, the time information obtained from the previous process (Part (a)) were used as the inputs. The AHI data selected for the SZM and RAM methods are illustrated in Figure 5. These data were then subjected to a compositing process. For each pixel, a single observation result from among the seven candidates was selected by comparing the apparent temperatures retrieved from the AHI band 14. This temperature comparison provided an initial cloud screening process. The screening algorithm is known as the Maximum apparent Temperature (MaT) [37] and can detect and screen observations influenced by clouds and cloud shadows. This approach provided two composite scenes: one using the SZM method, and the other using the RAM method. The rest of the process (described in the following sections) was performed only on the MODIS and AHI data listed in Tables 3 and 4 for each ROI.

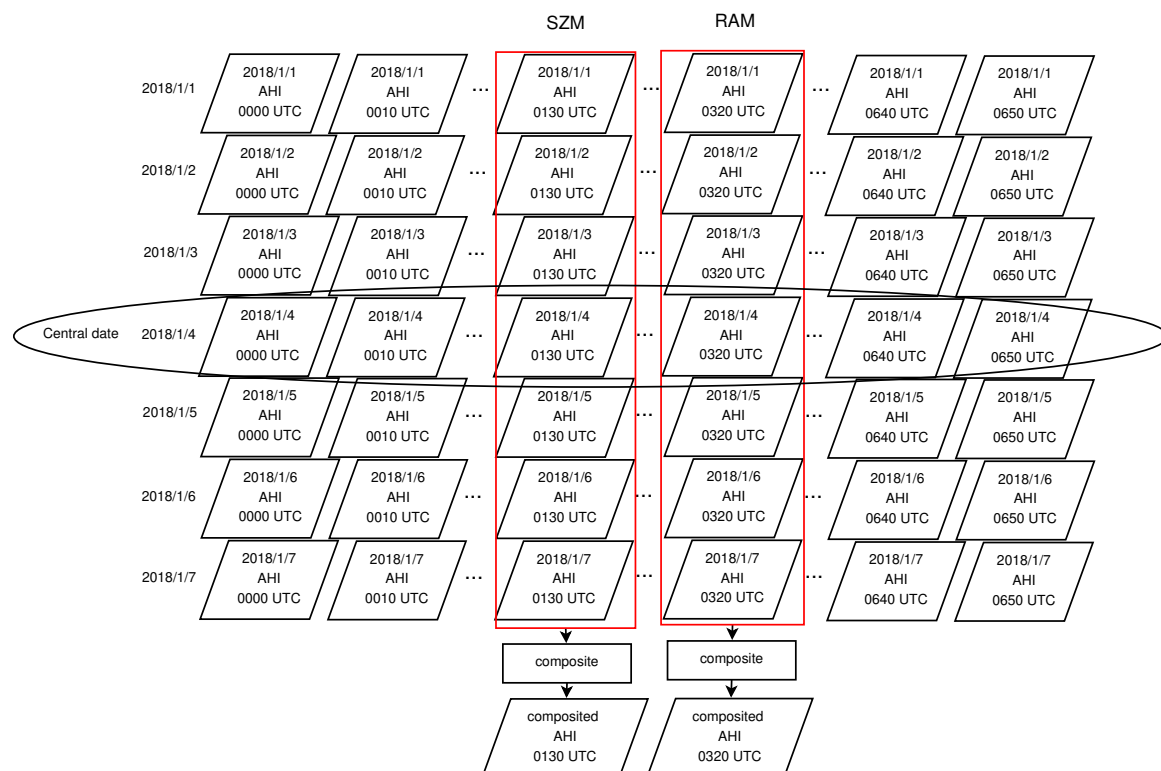


Figure 5. Overview of the AHI data composite. AHI data collected over seven consecutive days were used to create a single image for each of the SZM and RAM methods (for a total of two images). The SZM and RAM images differed with respect to the data acquisition time. The central date of the AHI observation period is the same as that designated for the MODIS data.

4.3. Atmospheric Corrections

Atmospheric corrections were performed to address molecular scattering and ozone absorption effects [29]. We decided to process the atmospheric corrections conservatively according to the methods

of Chang et al. [27] to avoid introducing artificial differences with over-corrections of the atmospheric influences. This study applied one algorithm to both the MODIS and AHI images in exactly the same way [29] to avoid introducing differences into the sensor data. Our correction scheme is relatively conservative compared to full atmospheric corrections that account for gaseous absorption and aerosol scattering. Note that these influences remained present in the compared data, denoted top-of-canopy (TOC) reflectances in this study. Differences arising from atmospheric corrections were effectively avoided by applying a common algorithm to the top-of-atmosphere (TOA) reflectances obtained from the MODIS and AHI sensors. The atmospheric corrections applied to the two sensors differed only with respect to the sensor-specific Spectral Response Functions (SRFs) used to compute look-up tables (LUTs) of the scattering and absorption cross-sections (wavelength-dependent optical depths). A series of particle transport simulations [38] was performed assuming spatially one-dimensional conditions (plane parallel) and two angular parameters, the S_{40} approximation [39]. We obtained the path radiance, bi-hemispherical reflectance, and transmittance as a function of the viewing and illumination angles, and the optical depth. These simulation results were then stored in LUTs as a function of those parameters [40]. The optical depth of the Rayleigh scattering was determined by the elevation of each pixel, which was interpolated from the digital elevation model of the Earth topography 5-min grid (ETOPO5) [41]. The ozone absorption correction was implemented using the absorption cross-sections stored in the 6S code [42] based on the values observed by the Aura/Ozone Monitoring Instrument (OMI) sensor [43]. In summary, Rayleigh scattering effects were corrected using the LUTs developed based on the pixel elevations interpolated from the ETOPO5. The ozone absorption effects were corrected based on the observation data reported by Aura/OMI.

4.4. Precise Cloud Screening

The pixels contaminated by clouds remained present in the composited AHI scenes. These artifacts were identified finally by visual inspection during the study. Prior to the visual inspection, cloud influences were removed from our comparison by conducting precise cloud screening based on the brightness temperature and reflectance data according to the methods reported by Ishida and Nakajima, and Shang et al. [44,45]. The AHI observation results were considered to be cloudy if at least either one of the conditions described in Equation (1) or (2) holds,

$$T_{b14} - T_{b7} \leq T_t, \quad (1)$$

$$v \leq v_t, \quad (2)$$

where T_{b7} and T_{b14} are the brightness temperature of the AHI bands 7 and 14, respectively. v represents the NDVI computed from the TOC reflectances of the AHI. T_t and v_t are the thresholds of the brightness temperature and NDVI, respectively. Note that we chose different values of T_t and v_t for the forest and urban areas. The cloud screening process using the brightness temperature was not applied to the urban areas. The land cover-dependent thresholds are summarized in Table 5. The pixels assumed to be cloudy were labeled for elimination from the AHI data. Furthermore, an additional cloud detection process was conducted over the remaining pixels (with no label). For this purpose, we computed the average and standard deviations of the red reflectances over the ROI. If at least one of the red reflectances in the AHI or MODIS data exceeded the average value over the ROI by twice the standard deviation, the observation was considered to be influenced by clouds.

Table 5. Thresholds (T_t and v_t) for the forest and urban ROIs.

	T_t	v_t
Forest	−6.5	0.470
Urban	-	−0.037

In summary, we performed cloud screening multiple times in different ways. For the MODIS data, we used the MOD35 QA flag (confident clear). For the AHI data, the MaT algorithm was employed as the initial screening process. Finally, algorithms based on the temperature and NDVI [44,45] and the red band thresholding were used to further filter out the cloud influence. Recall that red reflectance thresholding was used for both the MODIS and AHI data. Only the pairs of pixels remaining after the screening processes were compared in this study.

4.5. AHI-MODIS Data Match-Up

All pixels in the MODIS data within the ROIs were paired with the collocated pixels of the AHI data based on the nearest neighbor algorithm over the geographic coordinates. Pixel pairs containing cloudy pixels either or both the AHI and MODIS observations, as determined in the previous analysis step, were not used in the subsequent processes. Table 6 lists the number of pixels remaining after the AHI-MODIS data match-up over each ROI and using each pair selection method (SZM or RAM).

Note that the geolocation accuracy of the Terra MODIS was better than 45 m [46], whereas the AHI data were reported to be 150 m (north–south) \times 500 m (east–west) for band 3 (approximately 0.3×1.0 pixels, 500 m resolution) in the Japan Area product [47]. The geolocation errors in the satellite products influenced the reflectance comparisons to a lesser degree because at the image data spatial resolution (1 km), the ROIs of the two forest sites were considered to be homogeneous. By contrast, the urban areas used as reference sites for each forest ROI were not assumed to be homogeneous. The results introduced in subsequent sections support this assumption to some extent.

Table 6. Number of pixels paired for comparison after all screening processes had been applied. Dates are represented by six digits: “YYMMDD”.

KochiF	SZM	RAM	AichiF	SZM	RAM	KochiU	SZM	RAM	AichiU	SZM	RAM
180126	135	176	170125	190	178	180110	1	1	170125	8	8
170224	204	174	160208	186	194	170224	1	1	160208	10	11
160325	215	210	160327	200	191	170328	4	4	160311	7	7
170413	200	208	180402	39	46	170429	4	4	160412	2	2
160512	226	212	180520	32	32	160512	4	4	180520	7	7
180603	116	98	170602	8	8	-	-	-	170602	13	13
160731	107	10	150731	174	137	-	-	-	180723	37	36
180806	102	15	180808	192	125	180806	0	0	180808	38	36
160901	212	154	160903	188	197	160901	3	3	160903	2	2
151017	211	213	151003	178	180	151017	2	2	151019	6	7
171107	199	204	171109	119	225	171107	5	5	171125	23	22
171209	234	190	151222	173	76	171209	4	4	161208	25	17

4.6. Evaluation Method

As an indicator of the reflectance comparison, we employed the reflectance ratio between the corresponding bands of the two sensors. This ratio has been used in many studies, especially in time-trend analysis [48]. Because our comparisons were performed as a function of the DOY, we followed this standard approach for the comparison. The reflectance ratio ($r_{i,j}$) was defined by

$$r_{i,j} = \frac{\rho_{M,i,j}}{\rho_{A,i,j}}, \quad (3)$$

where the subscript i indicates the MODIS/AHI scene pixel number, and j is used to identify the date of data acquisition (scene identifier in this study). The subscripts M and A indicate the MODIS and AHI origin of the data, respectively. The arithmetic mean of $r_{i,j}$ is represented by \bar{r}_j and is computed using all available pixels remaining after applying the cloud screenings process to the j th scene. The area-averaged reflectances, \bar{r}_j , are considered to be “consistent” when \bar{r}_j is close to unity. Finally,

the consistency between the sensors in the paired j th scene is evaluated based on the difference from unity, E_j , defined by

$$E_j = |1 - \bar{r}_j|. \quad (4)$$

Inconsistencies between the sensors arise from a variety of factors. Among these factors, differences in the geometric conditions, such as the solar zenith and relative azimuth angles, are central to determining the consistency in this study. We analyzed the results based on differences in the geometric conditions. We denoted the differences in the solar zenith angles between the MODIS and AHI as d_{θ_j} . Similarly, differences in the relative azimuth angle are denoted by d_{ϕ_j} . These variables are defined as

$$d_{\theta_j} = \bar{\theta}_{M,j} - \bar{\theta}_{A,j}, \quad (5)$$

$$d_{\phi_j} = \bar{\phi}_{M,j} - \bar{\phi}_{A,j}, \quad (6)$$

where θ and ϕ represent differences in the solar zenith and relative azimuth angles, respectively. The area-averaged values of θ and ϕ are also defined by $\bar{\theta}$ and $\bar{\phi}$, respectively.

The reflectance ratio $r_{i,j}$ is used for not only actual data but also simulation data. Numerical simulations were performed to quantitatively examine the influences of the SRF differences between the MODIS and AHI data. A radiative transfer model, PROSAIL [49], was employed. The spectral reflectances of the AHI and MODIS were simulated by spectrally convolving the reflectances of the vegetation canopy with the SRFs for each band as a function of two parameters, namely, LAI and “psoil”, which is a blending coefficient of two distinctive soil spectra: dry and wet soil.

5. Results

The results of the AHI and MODIS reflectance comparisons are presented in Section 5.1. We conducted numerical simulations using a radiative transfer model of the vegetation canopy. This simulation evaluated the effects of the differences in the SRFs across the sensors: The SRF differences are especially significant in the green bands. We investigated the influence of the SRFs thoroughly to validate our results in Section 5.2.

5.1. Comparison Results Based on the Actual Data

Figure 6a,b show the reflectance ratios obtained using the SZM and RAM methods applied to the forests in Kochi, respectively. The ratios were plotted as a function of the DOY so that their seasonal variations could be observed in the figures. The circles represent the area-averaged ratios (\bar{r}_j) for four bands. The error bars indicate the standard deviation of the ratio ($r_{i,j}$). The error bars in Figure 6a,b for a DOY of 154 are larger than the error bars obtained on other DOYs. These results suggest the presence of a factor rendering the data unreliable. The influence of cloud cover was suspected, and visual inspection confirmed that cloud influence was indeed present in the MODIS screened data. Thus, special caution was needed to interpret the data for this specific DOY.

The SZM results shown in Figure 6a reveal that the average ratio \bar{r}_j varied from 0.5 to 1.8. The ratio tended to exceed unity over the period between DOYs 133 and 218 and tended to be lower than unity in other periods. This trend was investigated by plotting the differences between the sensor geometric conditions. In these figures, the empty square indicates differences in the solar zenith angles (d_{θ_j}), and the empty triangle indicates differences in the relative azimuth angles (d_{ϕ_j}). Recall that differences in the solar zenith angles (empty circles) were nearly zero for the SZM method. Differences in the relative azimuth angles varied significantly. The differences became especially large during the winter season. Thus, ratios far from unity for d_{ϕ_j} became large. This correlation raised questions about the screening strategy for the geometric conditions in the GEO-LEO comparison. These results suggest that the differences between the relative azimuth angles of the sensors was most likely a major factor in producing reflectance inconsistencies. This can be inferred from the RAM results, as shown in

Figure 6b. A comparison of Figure 6a,b reveals that the value of \bar{r}_j was closer to unity for the RAM method. This improvement was obtained by adjusting the relative azimuth angle in the RAM method.

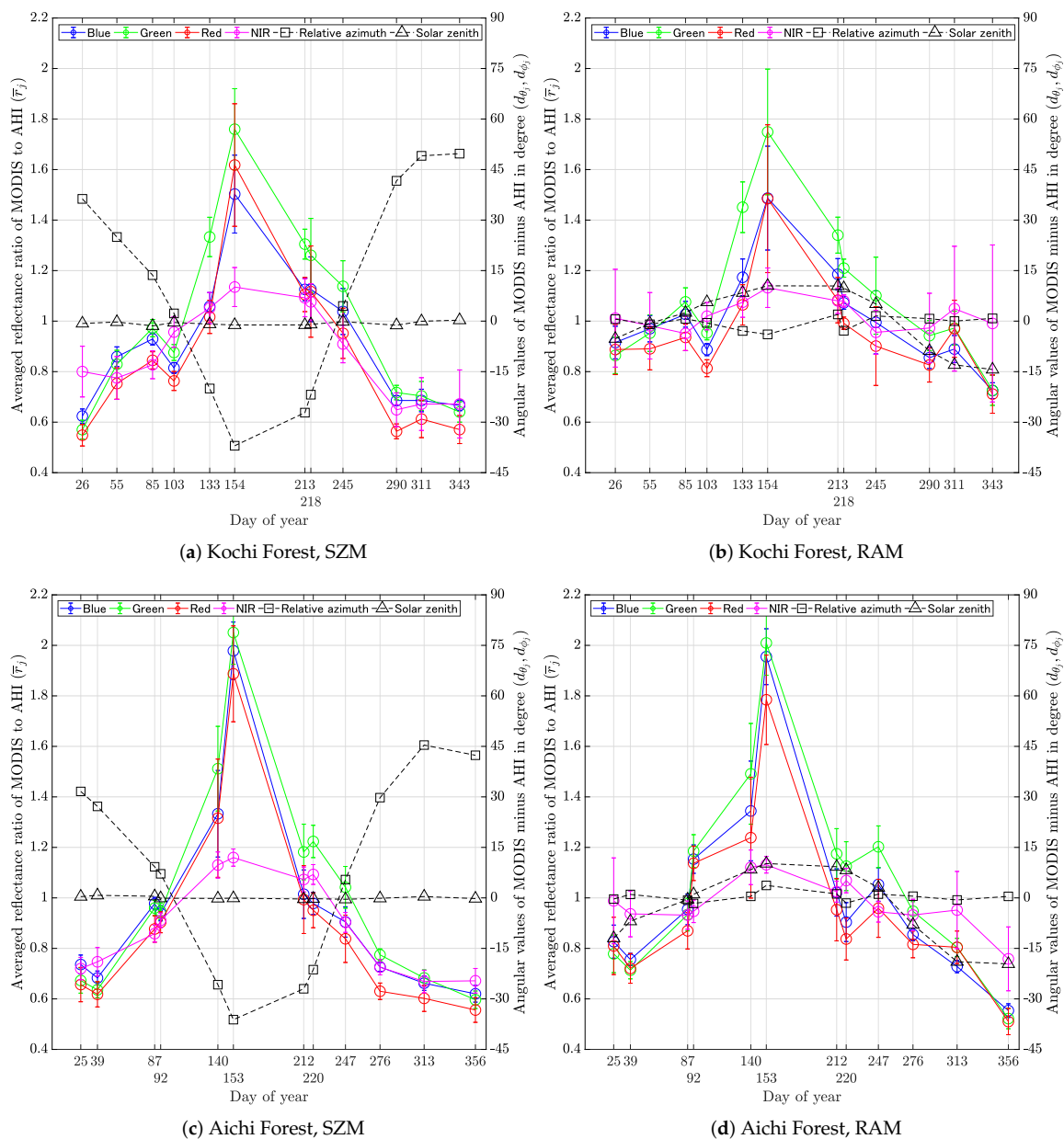


Figure 6. Area-averaged reflectance ratios (MODIS/AHI) in the four bands, by month. The upper two plots correspond to the Kochi Forest, SZM (a) and RAM (b). The lower two plots correspond to the Aichi Forest, SZM (c) and RAM (d). The differences between the MODIS and AHI solar zenith and relative azimuth angle observations are plotted on the secondary y-axis.

The reflectance inconsistencies displayed another notable trend in the green band variations. The ratios of the green bands were larger than the ratios of the other three bands, especially for DOYs 133–245. This was attributed to differences in the MODIS and AHI SRFs, which were numerically validated using an RT model (Section 5.2). By contrast, the smallest value of \bar{r}_j was the red band. The value mostly fell below 1.0, suggesting that the red band was also influenced by the SRF differences. This point is addressed in the following subsection.

The SZM and RAM results obtained in the Aichi Forest ROI (Figure 6c,d), showing trends in \bar{r}_j similar to those from Kochi. This means that, compared to the SZM method, the RAM method tends to select more consistent pair of reflectances between the two sensors.

We also compared the results of the SZM and RAM methods for the urban areas in Kochi and Aichi, as shown in Figure 7a,b, respectively. The value of \bar{r}_j obtained from the SZM method varied from 0.6 to 1.2, whereas the value obtained from the RAM method was closer to unity (0.8–1.3), except over certain dates (DOYs 119–245). Similar improvements were seen in the results obtained from the Aichi Urban ROI (Figure 7c,d). Interestingly, the band dependencies of the \bar{r}_j were much smaller, except in the blue band, than were observed over the forest targets. This result was attributed to the relatively flatter spectra of the urban surfaces compared to those of the forests. This trend was prominent in the green bands. The ratio of the green band did not exceed that of other bands during the summer season because less vegetation cover was present in the urban ROIs.

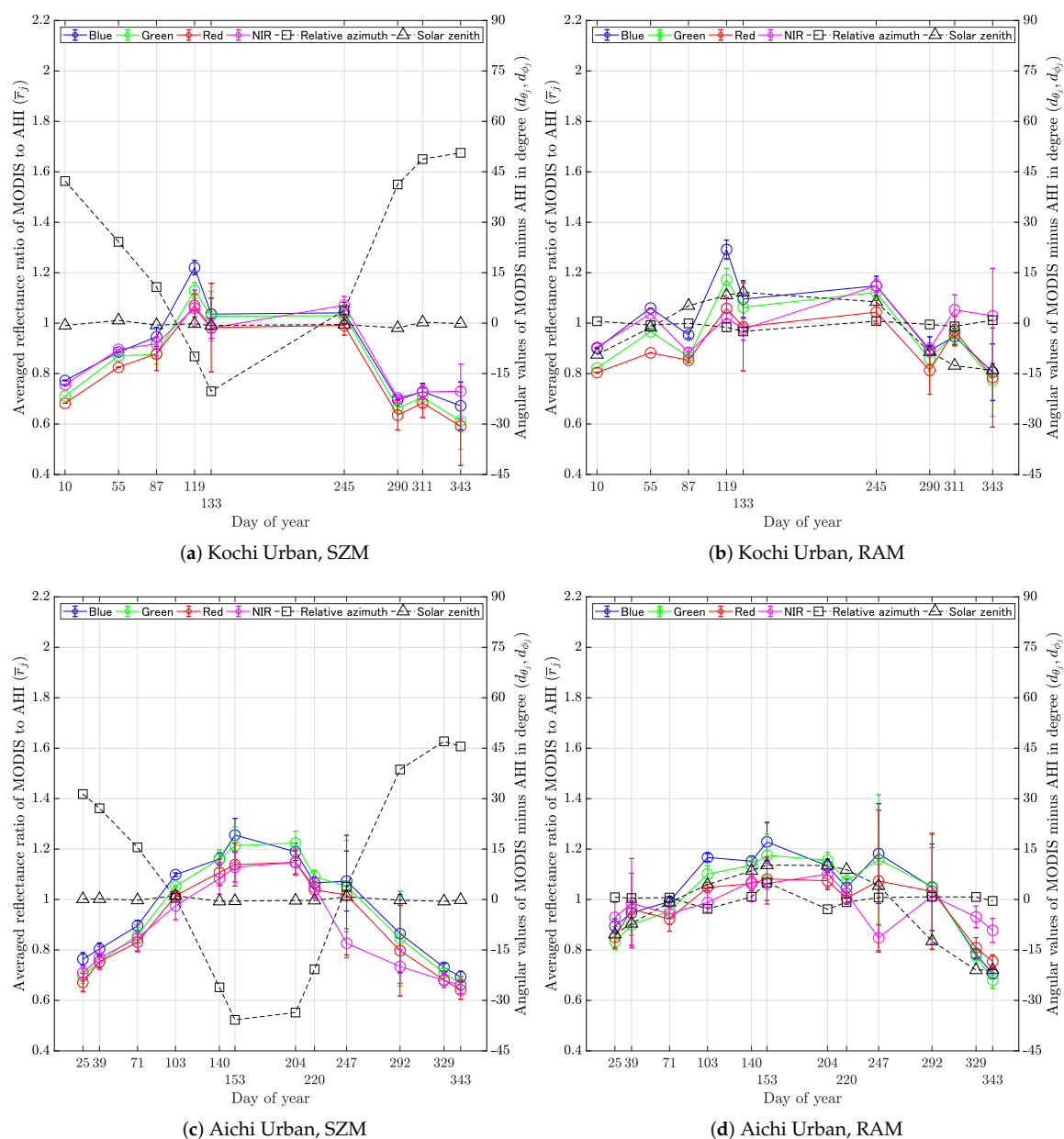


Figure 7. Area-averaged reflectance ratio (MODIS/AHI) for the urban ROIs. The upper two plots correspond to the Kochi Urban, SZM (a) and RAM (b). The lower two plots correspond to the Aichi Urban, SZM (c) and RAM (d).

Figure 8 shows the cumulative errors defined by the sum of E_j over the four bands for the SZM and RAM methods. The cumulative errors of the SZM and RAM methods are plotted side by side in the figure. Differences in the geometrical conditions (differences in the angles between the two sensors) are plotted on the secondary axis (right axis) as a function of the DOY. In these figures, a smaller absolute value indicates better agreement between the sensor reflectances or geometric conditions. The left bar with the solid lines shows the results obtained using the SZM method, and the right bar with the dashed lines shows the results obtained using the RAM method. The cumulative errors in the RAM method were smaller than those obtained in the SZM method, with a few exceptions (Figure 8a,b). This trend can also be seen in the urban ROI results (Figure 8c,d). These results indicate better consistency in the RAM results than in the SZM results. We compared the cumulative errors for the red and NIR bands in Figure 9. This comparison is mainly used for vegetation monitoring, and the red and NIR bands are used most frequently. These results confirmed that the selection of the reflectance pairs by the RAM method provided better consistency than selection by the SZM method.

As a summary of this subsection, we tabulated the results of our comparisons to confirm the trends described above. The SZM and RAM performance differences in E_j , defined by $|1 - \bar{r}_{j_{RAM}}| - |1 - \bar{r}_{j_{SZM}}|$, are summarized in Tables 7 and 8. The differences are tabulated based on band, month, and ROI. Note that the negative value in the tables indicates cases in which RAM provides better results (more consistent results) than SZM. In the table, the negative values are highlighted by color. A negative value occurred over 81% of the Kochi Forest, 69% of the Aichi Forest, 67% of the Kochi Urban Area, and 88% of the Aichi Urban Area. The results in October and November show especially large negative values, indicating greater improvement of the RAM method compared to the SZM method. Although positive cases occurred in a fair fraction of cases, the magnitudes of the positive values were smaller than the magnitudes of the negative values, except in the green band. These results suggest that the RAM method selected more consistent pairs of reflectances in most cases. The green band provided relatively large positive values, especially in the spring and summer seasons over the forest ROIs. This observation was attributed to SRF differences between the MODIS and AHI, as discussed in our previous study [29]. Special caution is needed when using green bands interchangeably. This point is further addressed in the following subsection.

Table 7. Summary of $|1 - \bar{r}_{j_{RAM}}| - |1 - \bar{r}_{j_{SZM}}|$ for the two forest ROIs. Negative values indicate a better performance of the RAM method than the SZM method.

KochiForest						AichiForest					
	Doy\Band	Blue	Green	Red	NIR	Doy\Band	Blue	Green	Red	NIR	
January	180126 (26)	−0.291	−0.294	−0.339	−0.188	170125 (25)	−0.091	−0.106	−0.153	−0.268	
February	170224 (55)	−0.111	−0.123	−0.137	−0.207	160208 (39)	−0.073	−0.078	−0.103	−0.190	
March	160325 (85)	−0.044	0.048	−0.091	−0.124	160327 (87)	0.023	0.026	0.007	−0.073	
April	170413 (103)	−0.072	−0.077	−0.051	−0.024	180402 (92)	0.093	0.132	0.040	−0.036	
May	160512 (133)	0.115	0.118	0.048	0.023	180520 (140)	0.011	−0.020	−0.077	−0.009	
June	180603 (154)	−0.016	−0.011	−0.133	−0.003	170602 (153)	−0.023	−0.041	−0.103	−0.028	
July	160731 (213)	0.060	0.036	−0.022	−0.012	150731 (212)	0.007	−0.007	0.040	−0.048	
August	180806 (218)	−0.053	−0.051	−0.108	0.004	180808 (220)	0.074	−0.098	0.114	−0.024	
September	160901 (245)	−0.033	−0.037	0.051	−0.046	160903 (247)	−0.042	0.160	−0.121	−0.042	
October	151017 (290)	−0.169	−0.225	−0.263	−0.324	151003 (276)	−0.128	−0.173	−0.186	−0.207	
November	171107 (311)	−0.204	−0.269	−0.357	−0.279	171109 (313)	−0.066	−0.121	−0.202	−0.283	
December	171209 (343)	−0.059	−0.086	−0.140	−0.319	151222 (356)	0.066	0.074	0.046	−0.087	
	Average	−0.073	−0.081	−0.129	−0.125	Average	−0.012	−0.021	−0.058	−0.108	
	Avg. (April–September)	0.000	−0.004	−0.036	−0.010	Avg. (April–September)	0.020	0.021	−0.018	−0.031	
	Avg. (Other)	−0.146	−0.158	−0.221	−0.240	Avg. (Other)	−0.045	−0.063	−0.099	−0.185	

Table 8. Summary of $|1 - \bar{r}_{j_{RAM}}| - |1 - \bar{r}_{j_{SZM}}|$ for the two urban ROIs. Negative values indicate that the RAM method performed better than the SZM method.

	KochiUrban					AichiUrban				
	Doy\Band	Blue	Green	Red	NIR	Doy\Band	Blue	Green	Red	NIR
January	180110 (10)	−0.128	−0.111	−0.122	−0.149	170125 (25)	−0.131	−0.137	−0.179	−0.220
February	170224 (55)	−0.055	−0.096	−0.057	−0.067	160208 (39)	−0.143	−0.147	−0.208	−0.217
March	170328 (87)	−0.008	0.008	0.026	0.034	160311 (71)	−0.096	−0.095	−0.093	−0.097
April	170429 (119)	0.072	0.043	−0.011	−0.038	160412 (103)	0.068	0.048	0.033	−0.013
May	160512 (133)	0.059	0.035	−0.003	0.005	180520 (140)	−0.009	−0.025	−0.045	−0.013
June	-	-	-	-	-	170602 (153)	−0.027	−0.038	−0.056	−0.065
July	-	-	-	-	-	180723 (204)	−0.056	−0.068	−0.073	−0.047
August	-	-	-	-	-	180808 (220)	−0.017	−0.017	−0.033	−0.025
September	160901 (245)	0.107	0.093	0.035	0.077	160903 (247)	0.109	0.105	0.055	−0.022
October	151017 (290)	−0.196	−0.194	−0.178	−0.192	151019 (292)	−0.087	−0.103	−0.170	−0.251
November	171107 (311)	−0.218	−0.250	−0.285	−0.220	171125 (329)	−0.053	−0.068	−0.128	−0.252
December	171209 (343)	−0.133	−0.160	−0.193	−0.241	161208 (343)	−0.012	−0.015	−0.113	−0.216
	Average	−0.056	−0.070	−0.088	−0.088	Average	−0.038	−0.047	−0.084	−0.120
	Avg. (April–September)	0.079	0.057	0.007	0.015	Avg. (April–September)	0.011	0.001	−0.020	−0.031
	Avg. (Other)	−0.123	−0.134	−0.135	−0.139	Avg. (Other)	−0.087	−0.094	−0.149	−0.209

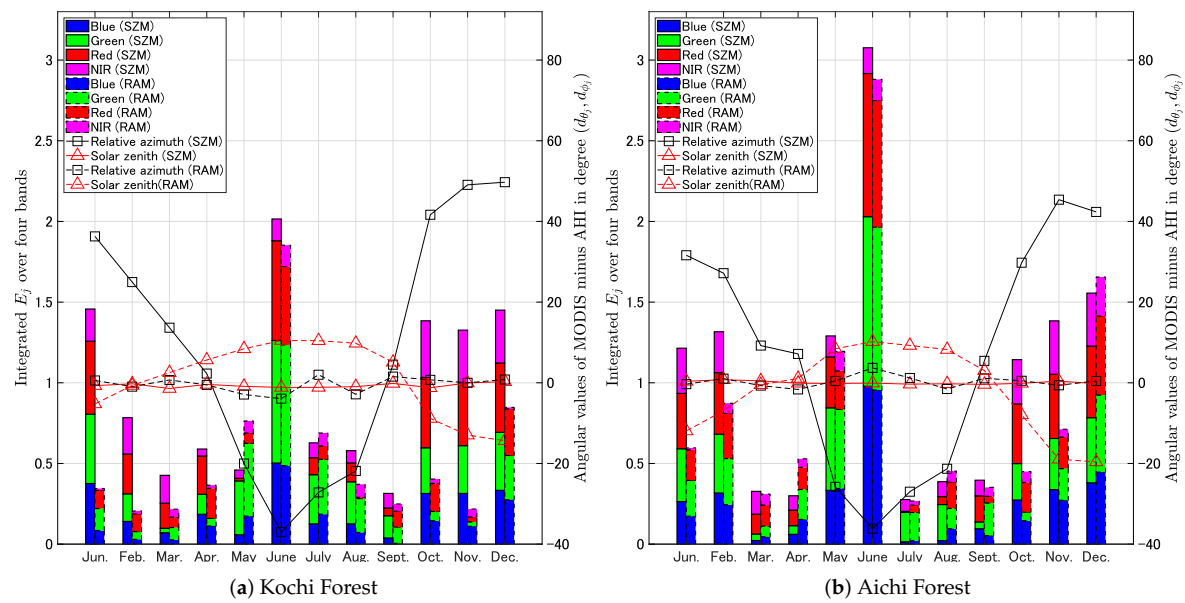


Figure 8. Cont.

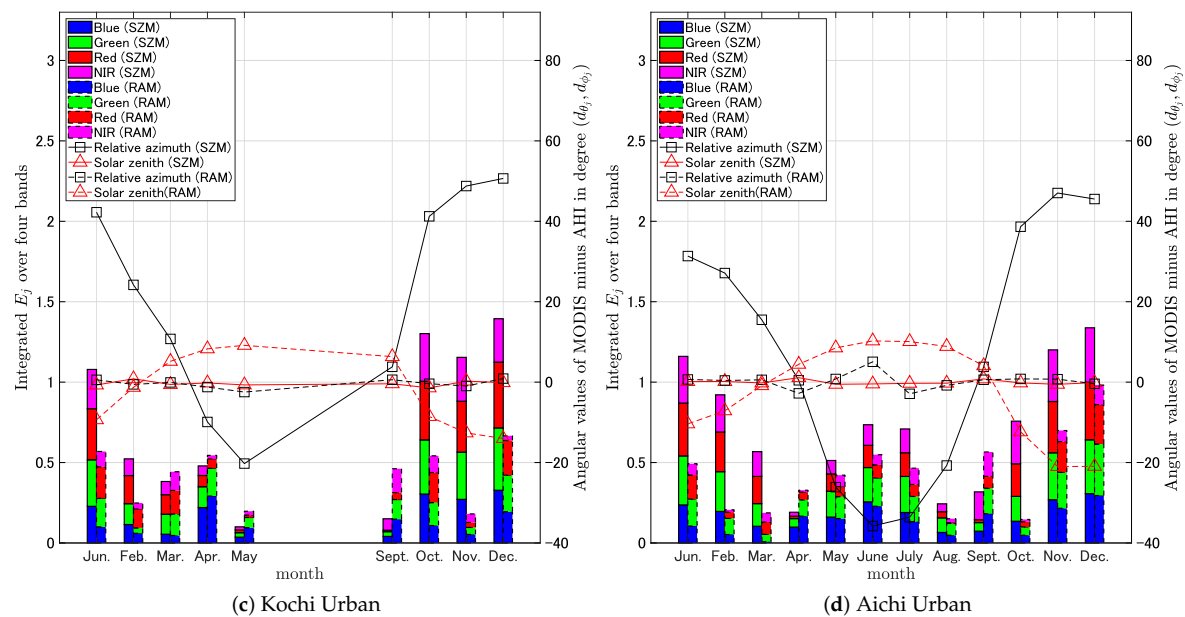


Figure 8. Integrated values of $E_j = |1 - \bar{r}_j|$ over the four bands, obtained using the SZM and RAM methods. Differences in the MODIS and AHI relative azimuth angles and solar zenith angles are plotted on the secondary y-axis: (a) Kochi Forest; (b) Aichi Forest; (c) Kochi Urban; and (d) Aichi Urban.

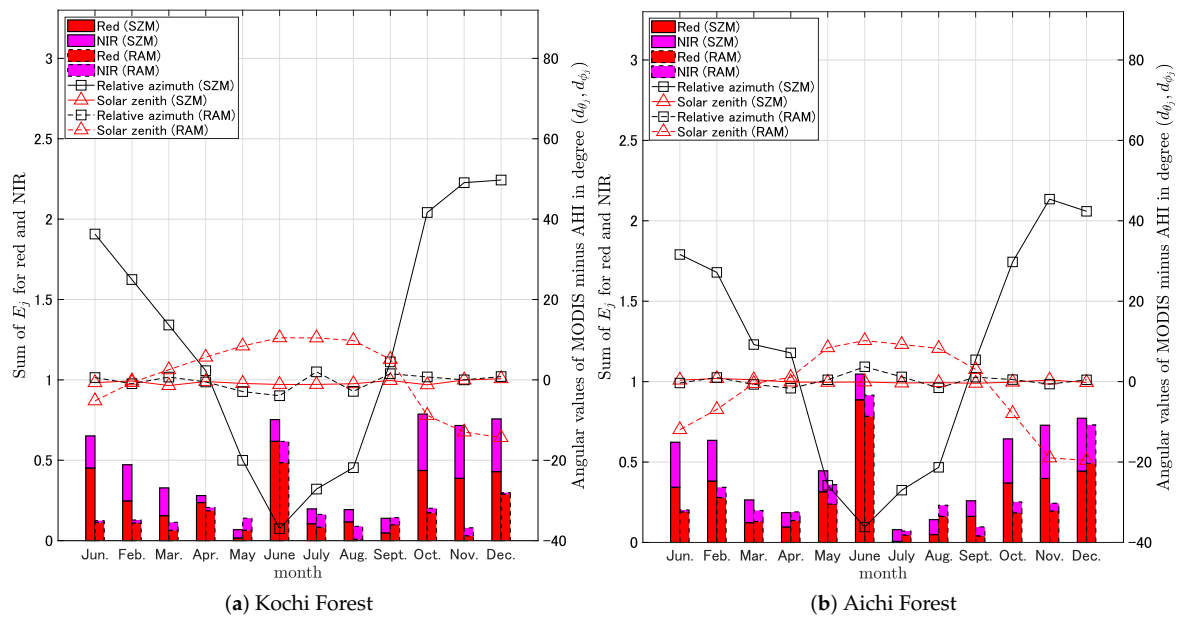


Figure 9. Cont.

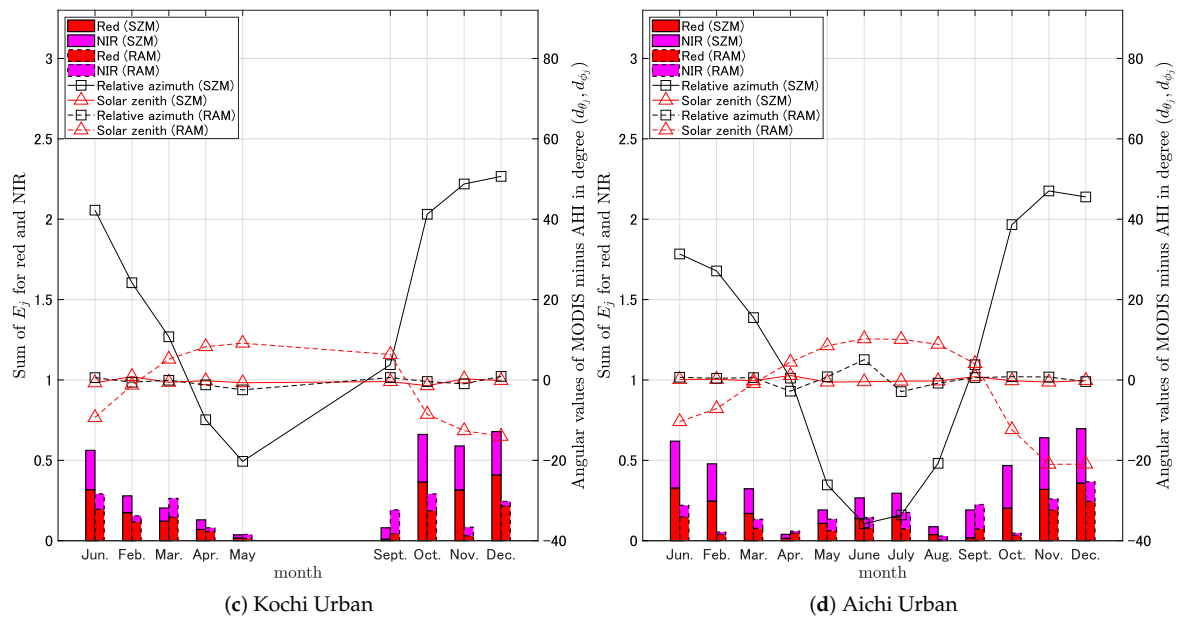


Figure 9. Same plot (E_j) as shown in Figure 8, but only over the red and NIR bands: (a) Kochi Forest; (b) Aichi Forest; (c) Kochi Urban; and (d) Aichi Urban.

5.2. Simulation Results by an RT Model

Figure 10 shows the SRFs of the two sensors and simulated reflectances of each band on the vegetation. The input parameters of the model assumed in this study are summarized in Table 9. In the figure, note that the SRFs of the green bands differ to a greater extent than the SRFs of the other three bands. The SRF of the AHI green band is located below the green spectral peak of the canopy spectrum. By contrast, the SRF of the MODIS green band is located on the green peak. This SRF difference could be the cause of the effects observed in the previous subsection.

The simulated reflectance ratios are shown as contour plots in Figure 11. The ratios were close to 1.0 in the blue and NIR bands (Figure 11a,d). The ratio in the red band reached 0.9, larger than the value, 1.0, obtained in the blue and NIR bands. By contrast, the ratio of the green band (Figure 11b) was

far higher than 1.0: The maximum value even reached 2.0 in the simulation. Note that the green band ratio increased as the LAI increased. This suggested that the green band ratio for the forest ROI tended to be higher than for the urban ROI. This also suggested that the ratio tended to be highest during the summer. This trend corresponded very well to the results obtained from the data comparisons. As mentioned in the previous subsection, relatively large values of the green band ratios (1.1–1.8) were observed over the forest ROIs (Figure 6) during the spring through the fall. This effect was observed especially during the summer. Thus, the simulation confirmed our interpretation of the results. In addition to the green band trend, a similar trend was observed in the red band ratio. The low value of the red band ratio (0.9–1.0) in the simulation (Figure 11c) corresponded well with the trends shown in the previous subsection (e.g., Figure 6a,b). In those figures, the red band ratio tended to be lower than that of the other bands. These results indicated that the red band consistency was influenced by the SRF differences, to a certain extent.

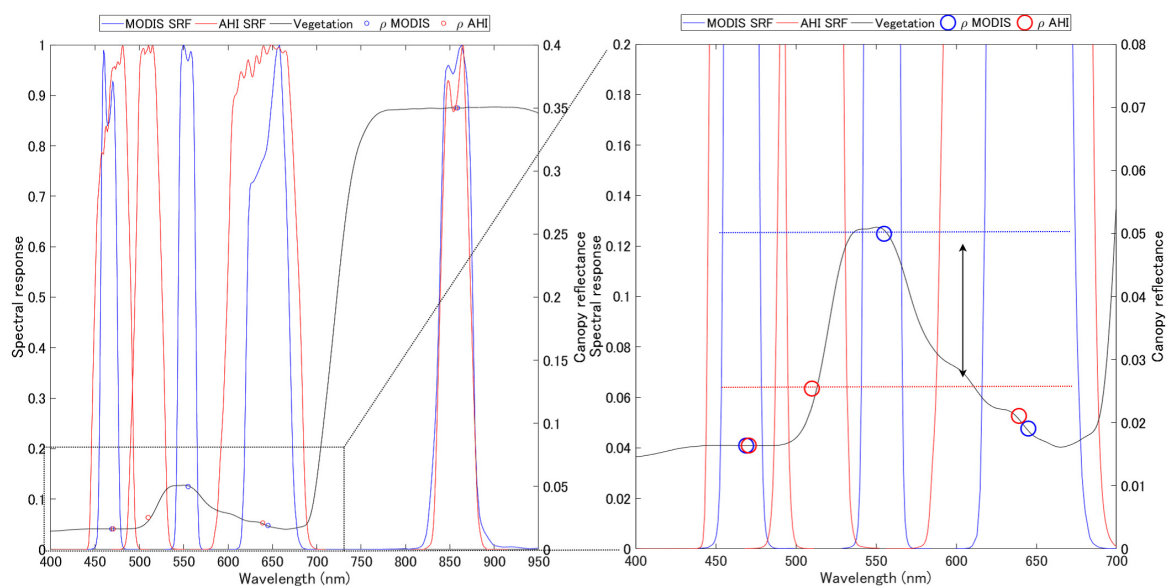


Figure 10. SRFs for the AHI and MODIS, and spectral reflectances of the vegetation canopy simulated using PROSAIL. The values of LAI and ρ_{soil} were assumed to be 2.5 and 0.0, respectively. Circles indicate the spectrally convoluted reflectances using SRFs. In the green bands, reflectance differences between AHI and MODIS were greater than in the other bands.

Table 9. Input parameters for the PROSAIL algorithm used in the numerical simulations. The LIDF is the leaf inclination distribution function. The parameter ρ_{soil} was used to describe the moisture-induced reflectance changes in the soil surface (from wet to dry).

Canopy	
LAI	0.0 (1.0×10^{-9}) to 5.0 with 0.5 increment
LIDF (ID4LIDF)	Planophile
Hotspot size parameter (hspot)	0.01
Leaf structure parameter (N)	1.5
Chlorophyll content (Cab)	40 $\mu\text{g}/\text{cm}^2$
Carotenoid content (Car)	8 $\mu\text{g}/\text{cm}^2$
Brown pigment content (Cbrown)	0.0 (unitless, fraction)
Geometry	
Equivalent water thickness (Cw)	0.01 cm
Dry matter content (Cm)	0.009 g/cm^2
ρ_{soil}	0.0–1.0 with 0.1 increment
Solar zenith angle (tts)	30.0 deg
Viewing zenith angle (tto)	40.0 deg
Relative azimuth angle (psi)	36.0 deg

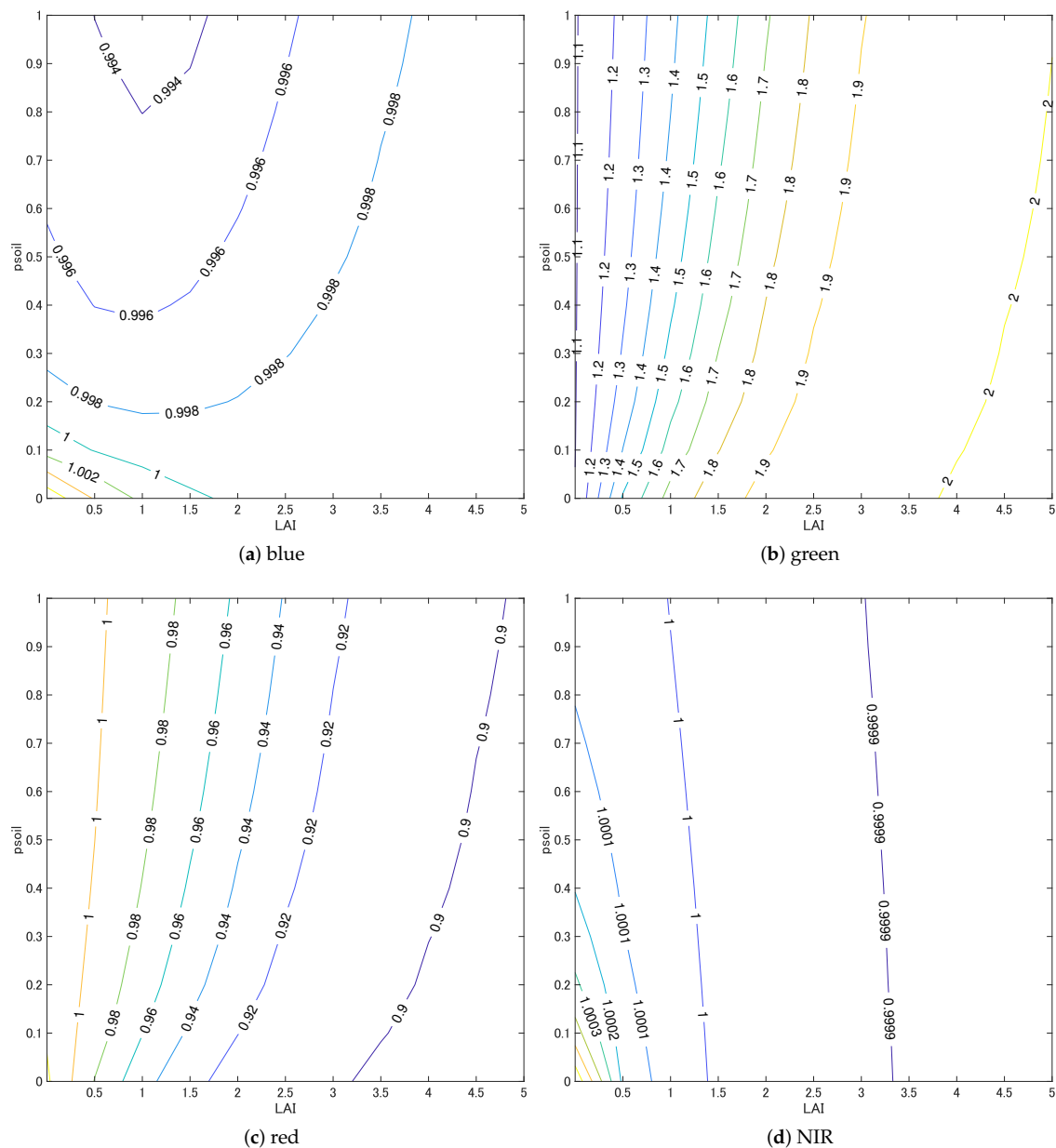


Figure 11. Contour plots of the simulated MODIS to AHI reflectance ratios for (a) blue, (b) green, (c) red, and (d) NIR bands as a function of LAI and soil moisture surface effects. Ratios were close to 1.0 in the blue and NIR bands, whereas ratios were much higher than 1.0 in the green band and were smaller than 1.0 in the red band.

6. Discussion

The results obtained from the data comparisons (Section 5.1) indicate that the ratio in the green band was higher than the ratios in the other bands, especially during the spring and summer seasons. Interestingly, this trend was not observed during other periods. This effect must be strongly related to both the photosynthetic activities of the vegetation canopy, i.e., the coniferous forests [50], and to differences in the SRFs of the green band. This trend suggests that the reflectance consistency depends on the land cover. A similar dependence could be seen in the red band. The reflectance ratio of the red band tended to be lower than that of the other bands. These trends agreed well with the numerical simulation results, suggesting that a reduction in these influences could require prior knowledge of the vegetation quantity. This perspective raises another question to be addressed in the future.

The RAM method did not always provide more consistent comparisons than the SZM method. This could be seen during the summer. In this season, the solar zenith angle was small (close to its nadir). When the solar zenith angle becomes small, the influence of the relative azimuth angle tends to be small. Thus, adjustments to the relative azimuth angle using the RAM method are less significant. By contrast, the RAM method selected AHI data acquired at different times than the MODIS data, which introduced differences in the solar zenith angles of the MODIS and AHI data. During the summer, differences (in the solar zenith angle) reached 10° from May to August, resulting in an even worse performance by the RAM method than by the SZM method.

Moreover, the performance loss of the RAM method was caused by the relatively early sunset around the winter solstice. The RAM method selected AHI data observed at later hours of the day during the winter. The observation time of RAM for the latest case reached 06:50 UTC (15:50 local time), as shown in Table 4. The time to sunset (Table 10) was only 1 h from the data acquisition time (07:45 UTC). Because the illumination conditions were shifted toward twilight, the atmosphere exerted a greater influence on the data. For these reasons, the RAM method was limited around the winter solstice.

Around the winter solstice, the illumination conditions selected by the SZM and RAM methods were largely different. This result was confirmed by plotting the reflectance ratios as a function of time over the entire day time. Figure 12a,b show the results of the reflectance ratios \bar{r}_j obtained from the Aichi Forest on 9 November 2017 and 22 December 2015, respectively. The times selected using the SZM and RAM methods are indicated by a solid line and a dashed line, respectively. The ratio of the data selected using the RAM method approached unity on 9 November 2017 (Figure 12a), whereas the influence of the illumination conditions was observed on 22 December 2015 (Figure 12b).

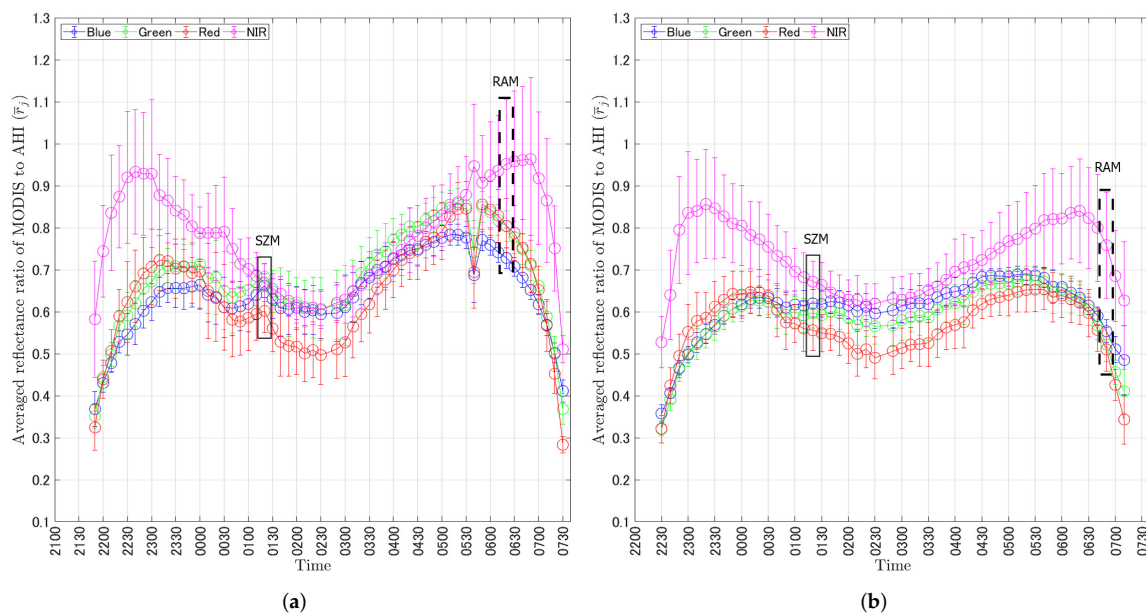


Figure 12. The \bar{r}_j values for four bands along the UTC time, from sunrise to sunset, calculated using composite data collected using the algorithm described in Section 4.2: (a) AichiForest on 9 November 2017; and (b) AichiForest on 22 December 2015. Rectangles depicted by the solid and dashed lines indicate the times selected using the SZM and RAM methods, respectively.

The RAM method tended to perform better than the SZM method during winter, except around the winter solstice. This was attributed to the relatively significant influence of the relative azimuth angle compared to the solar zenith angle. During winter, the solar zenith angle was so large that the influence caused by the difference in the relative azimuth angle became significant. Thus, the choice of the relative azimuth angle became more important than the choice of the solar zenith angle. This could

explain the significant improvement in the SZM performance compared to the RAM performance during winter.

In addition to the influences of the geometric conditions and biophysical parameters, several other factors may have influenced the reflectance ratios: terrain and shadow effects, atmospheric conditions, BRDF, and rotational asymmetry. These factors may degrade the performance of the RAM method compared to the SZM method. Although thorough investigations are needed to identify the influences of each factor, such investigations may have trouble evaluating these influences independently. These influences are mutually related in a complex manner and differ from region to region. For instance, terrain effects are induced by differences in the solar zenith angle, view zenith, azimuth angle, and relative azimuth angle. Therefore, investigations into the evaluation methodology itself could be useful for GEO-LEO inter-comparisons of middle latitude regions.

Considering the measurement of the relative azimuth angle in the RAM method, two choices of rotational direction are available, namely, clockwise and counter-clockwise from the position of the AHI. In this study, we chose the clockwise measure for the relative azimuth angle to make the rotational direction identical to the one used for the MODIS observation. Selection of the counter-clockwise direction would have selected AHI data collected before sunrise during the winter. Thus, the choice of the clockwise angle was a requisite. Another advantage of this choice is that the number of available datasets is greater than for the counter-clockwise alternative, within the ROIs used in this study. The maximum value of the azimuth angle relative to the illumination angle at sunset is larger than the maximum value relative to the illumination angle at sunrise. For instance, over the ROI of Kochi city, 51 datasets are available on the summer solstice if we choose the clockwise angle. By contrast, only 33 datasets are available for the alternative choice (counter-clockwise). Similar trends were observed over all of the ROIs on the summer and winter solstices, as summarized in Table 10. Finally, the better choice of rotational direction for the relative azimuth angle depended on the geolocation and overpass time of a LEO satellite. Further investigations are needed to address this issue.

Table 10. Sunrise and Sunset times in the ROIs during the summer and winter solstices [51]. Dates are represented by six digits: “YYMMDD”.

	Sunrise Time	Sunset Time
Aichi (Nagoya) 180621	180620 19:38 UTC (180621 4:38 JST)	180621 10:10 UTC (180621 19:10 JST)
Aichi (Nagoya) 171222	171221 21:57 UTC (171222 6:57 JST)	171222 07:45 UTC (171222 16:45 JST)
Kochi (Kochi) 180621	180620 19:56 UTC (180621 4:56 JST)	180621 10:19 UTC (180621 19:19 JST)
Kochi (Kochi) 171222	171221 22:06 UTC (171222 7:06 JST)	171222 08:02 UTC (171222 17:02 JST)

7. Conclusions

This study proposed a data screening method, the Relative Azimuthal-angle Matching (RAM) method. The RAM method is a straightforward but unique technique for comparing GEO-LEO reflectances over forest targets located in middle latitude regions. The performance of the RAM method was validated by comparing the RAM results with those derived using the Solar Zenith-angle Matching (SZM) method. Data collected over three years were compared after processing using the RAM and SZM algorithms. The experimental results show that, in general, RAM was better than SZM throughout the year, except for the summer and a short period around the winter solstice. Especially in the autumn and winter, RAM outperformed SZM. These results were attributed to improvements in the relative azimuth angle by the RAM. The initial screening step used for GEO-LEO comparisons benefitted when the RAM method selected reflectance pairs with a smaller bias than the SZM method. This conclusion contradicts the intuition that simultaneous observations (SZM) would select better observation pairs. This study raises questions about the choice of screening criteria for middle latitude targets in the context of GEO-LEO comparison frameworks. Since our target ROIs were two similar mountainous forests with urban ROIs residing in each forest ROI, it was unrealistic to reach a definitive conclusion from the limited number of samples. Further studies will be needed to draw general

conclusions on the advantage of RAM over SZM. Further studies are needed to clarify the limitations of the RAM method as a function of the data acquisition time, geolocation of the targets, and sensor pairs. Moreover, extending the discussion to higher level of data products such as spectral vegetation indices and biophysical parameters will also be needed to further examine the differences between RAM and SZM in the context of GEO-LEO inter-comparison.

Differences between the SRFs of the MODIS and AHI datasets were investigated using numerical simulations. The green band ratio was large compared to the results obtained in the other bands. We concluded that this result arose from differences in the SRFs of the two sensors. Furthermore, the red ratio was influenced to some extent by SRF differences. These influences depended on the value of the LAI, suggesting at the reflectance comparison depended on land cover and seasonal variations. This dependence should be corrected by accounting for the LAI level. This issue should be addressed thoroughly in the future.

Author Contributions: Conceptualization, H.Y.; methodology, Y.A.; software, Y.A., R.K. and H.Y.; validation, Y.A., R.K., K.O., and H.Y.; formal analysis, Y.A.; investigation, Y.A.; resources, H.Y.; data curation, Y.A.; writing—original draft preparation, Y.A.; writing—review and editing, K.O. and H.Y.; visualization, Y.A. and R.K.; supervision, K.O. and H.Y.; project administration, H.Y.; and funding acquisition, Y.A. and H.Y.

Funding: This work was supported by Grant-in-Aid for JSPS Research Fellow Grant Number JP18J23448 (YA), JSPS KAKENHI Grant number JP15H02856 and JP17K07843 (HY).

Acknowledgments: We would like to thank Kenta Taniguchi for his contributions to the discussion. Himawari-8 Standard Data used in this research were produced by the NICT Science Cloud at National Institute of Information and Communications Technology. The Terra/MODIS datasets MOD021KM [32], MOD03 [33], MOD15A2H [30] and MOD35 [36] were acquired from the Level-1 and Atmosphere Archive & Distribution System (LAADS) Distributed Active Archive Center (DAAC), located in the Goddard Space Flight Center in Greenbelt, Maryland (<https://ladsweb.nascom.nasa.gov/>). The high-Resolution Land Use and Land Cover (HRLULC) map used in this study was produced by JAXA.

Conflicts of Interest: The authors declare no conflict of interest.

Abbreviations

The following abbreviations are used in this manuscript:

GEO	Geostationary Earth Observing
LEO	Low Earth Orbit
RAM	Relative Azimuthal-angle Matching
SZM	Solar Zenith-angle Matching
NDVI	Normalized Difference Vegetation Index
LAI	Leaf Area Index
ROI	Region Of Interest
MaT	Maximum apparent Temperature
DOY	Day Of Year
TOC	Top Of Canopy
TOA	Top Of Atmosphere
AHI	Advanced Himawari Imager
MODIS	Moderate Resolution Imaging Spectroradiometer
SRF	Spectral Response Function
ETOPO5	Earth topography 5-min grid
OMI	Ozone Monitoring Instrument

References

1. Schmit, T.J.; Lindstrom, S.S.; Gerth, J.J.; Gunshor, M.M. Applications of the 16 Spectral Bands on the Advanced Baseline Imager (ABI). *J. Oper. Meteorol.* **2018**, *6*, 33–46. [[CrossRef](#)]
2. Xie, Z.; Song, W.; Ba, R.; Li, X.; Xia, L. A Spatiotemporal Contextual Model for Forest Fire Detection Using Himawari-8 Satellite Data. *Remote Sens.* **2018**, *10*, 1992. [[CrossRef](#)]

3. Hally, B.; Wallace, L.; Reinke, K.; Jones, S.; Engel, C.; Skidmore, A. Estimating Fire Background Temperature at a Geostationary Scale—An Evaluation of Contextual Methods for AHI-8. *Remote Sens.* **2018**, *10*, 1368. [\[CrossRef\]](#)
4. Zhang, P.; Zhu, L.; Tang, S.; Gao, L.; Chen, L.; Zheng, W.; Han, X.; Chen, J.; Shao, J. General Comparison of FY-4A/AGRI with Other GEO/LEO Instruments and Its Potential and Challenges in Non-meteorological Applications. *Front. Earth Sci.* **2019**, *6*, 224. [\[CrossRef\]](#)
5. Yan, D.; Zhang, X.; Nagai, S.; Yu, Y.; Akitsu, T.; Nasahara, K.N.; Ide, R.; Maeda, T. Evaluating land surface phenology from the Advanced Himawari Imager using observations from MODIS and the Phenological Eyes Network. *Int. J. Appl. Earth Obs. Geoinf.* **2019**, *79*, 71–83. [\[CrossRef\]](#)
6. Bessho, K.; Date, K.; Hayashi, M.; Ikeda, A.; Imai, T.; Inoue, H.; Kumagai, Y.; Miyakawa, T.; Murata, H.; Ohno, T.; et al. An Introduction to Himawari-8/9—Japan’s New-Generation Geostationary Meteorological Satellites. *J. Meteorol. Soc. Jpn.* **2016**, *94*, 151–183. [\[CrossRef\]](#)
7. Schmit, T.J.; Griffith, P.; Gunshor, M.M.; Daniels, J.M.; Goodman, S.J.; Lebair, W.J. A Closer Look at the ABI on the GOES-R Series. *Bull. Am. Meteorol. Soc.* **2017**, *98*, 681–698. [\[CrossRef\]](#)
8. Fensholt, R.; Sandholt, I.; Stisen, S.; Tucker, C. Analysing NDVI for the African continent using the geostationary meteosat second generation SEVIRI sensor. *Remote Sens. Environ.* **2006**, *101*, 212–229. [\[CrossRef\]](#)
9. Fensholt, R.; Anyamba, A.; Stisen, S.; Sandholt, I.; Pak, E.; Small, J. Comparisons of Compositing Period Length for Vegetation Index Data from Polar-orbiting and Geostationary Satellites for the Cloud-prone Region of West Africa. *Photogramm. Eng. Remote Sens.* **2007**, *73*, 297–309. [\[CrossRef\]](#)
10. Fensholt, R.; Huber, S.; Proud, S.R.; Mbow, C. Detecting Canopy Water Status Using Shortwave Infrared Reflectance Data From Polar Orbiting and Geostationary Platforms. *IEEE J. Sel. Top. Appl. Earth Obs. Remote Sens.* **2010**, *3*, 271–285. [\[CrossRef\]](#)
11. Nigam, R.; Bhattacharya, B.K.; Gunjal, K.R.; Padmanabhan, N.; Patel, N.K. Formulation of Time Series Vegetation Index from Indian Geostationary Satellite and Comparison with Global Product. *J. Indian Soc. Remote Sens.* **2012**, *40*, 1–9. [\[CrossRef\]](#)
12. Kumar, P.; Bhattacharya, B.K.; Pal, P. Impact of vegetation fraction from Indian geostationary satellite on short-range weather forecast. *Agric. For. Meteorol.* **2013**, *168*, 82–92. [\[CrossRef\]](#)
13. Yan, D.; Zhang, X.; Yu, Y.; Guo, W. A Comparison of Tropical Rainforest Phenology Retrieved From Geostationary (SEVIRI) and Polar-Orbiting (MODIS) Sensors Across the Congo Basin. *IEEE Trans. Geosci. Remote Sens.* **2016**, *54*, 4867–4881. [\[CrossRef\]](#)
14. Yeom, J.M.; Jeong, S.; Jeong, G.; Ng, C.T.; Deo, R.C.; Ko, J. Monitoring paddy productivity in North Korea employing geostationary satellite images integrated with GRAMI-rice model. *Sci. Rep.* **2018**, *8*, 16121. [\[CrossRef\]](#)
15. Doelling, D.; Minnis, P.; Nguyen, L. Calibration comparison between SEVIRI, MODIS and GOES data. In Proceedings of the 2004 MSG RAO Workshop, Salzburg, Austria, 9–10 September 2004.
16. Doelling, D.R.; Haney, C.O.; Scarino, B.R.; Gopalan, A.; Bhatt, R. Improvements to the Geostationary Visible Imager Ray-Matching Calibration Algorithm for CERES Edition 4. *J. Atmos. Ocean. Technol.* **2016**, *33*, 2679–2698. [\[CrossRef\]](#)
17. Chander, G.; Hewison, T.J.; Fox, N.; Wu, X.; Xiong, X.; Blackwell, W.J. Overview of Intercalibration of Satellite Instruments. *IEEE Trans. Geosci. Remote Sens.* **2013**, *51*, 1056–1080. [\[CrossRef\]](#)
18. Fan, X.; Liu, Y. Multisensor Normalized Difference Vegetation Index Intercalibration: A comprehensive overview of the causes of and solutions for multisensor differences. *IEEE Geosci. Remote Sens. Mag.* **2018**, *6*, 23–45. [\[CrossRef\]](#)
19. Minnis, P.; Doelling, D.R.; Nguyen, L.; Miller, W.F.; Chakrapani, V. Assessment of the Visible Channel Calibrations of the VIRS on TRMM and MODIS on Aqua and Terra. *J. Atmos. Ocean. Technol.* **2008**, *25*, 385–400. [\[CrossRef\]](#)
20. Miura, T.; Muratsuchi, J.; Vargas, M. Assessment of cross-sensor vegetation index compatibility between VIIRS and MODIS using near-coincident observations. *J. Appl. Remote Sens.* **2018**, *12*, 045004. [\[CrossRef\]](#)
21. Heidinger, A.K.; Cao, C.; Sullivan, J.T. Using Moderate Resolution Imaging Spectrometer (MODIS) to calibrate advanced very high resolution radiometer reflectance channels. *J. Geophys. Res. Atmos.* **2002**, *107*, AAC11-1–AAC11-10. [\[CrossRef\]](#)

22. Cao, C.; Weinreb, M.; Xu, H. Predicting simultaneous nadir overpasses among polar-orbiting meteorological satellites for the intersatellite calibration of radiometers. *J. Atmos. Ocean. Technol.* **2004**, *21*, 537–542. [\[CrossRef\]](#)
23. Doelling, D.R.; Scarino, B.R.; Morstad, D.; Gopalan, A.; Bhatt, R.; Lukashin, C.; Minnis, P. The Intercalibration of Geostationary Visible Imagers Using Operational Hyperspectral SCIAMACHY Radiances. *IEEE Trans. Geosci. Remote Sens.* **2013**, *51*, 1245–1254. [\[CrossRef\]](#)
24. Cao, C.; Luccia, F.J.D.; Xiong, X.; Wolfe, R.; Weng, F. Early On-Orbit Performance of the Visible Infrared Imaging Radiometer Suite Onboard the Suomi National Polar-Orbiting Partnership (S-NPP) Satellite. *IEEE Trans. Geosci. Remote Sens.* **2014**, *52*, 1142–1156. [\[CrossRef\]](#)
25. Yu, F.; Wu, X. Radiometric Inter-Calibration between Himawari-8 AHI and S-NPP VIIRS for the Solar Reflective Bands. *Remote Sens.* **2016**, *8*, 165. [\[CrossRef\]](#)
26. Qin, Y.; McVicar, T.R. Spectral band unification and inter-calibration of Himawari AHI with MODIS and VIIRS: Constructing virtual dual-view remote sensors from geostationary and low-Earth-orbiting sensors. *Remote Sens. Environ.* **2018**, *209*, 540–550. [\[CrossRef\]](#)
27. Chang, T.; Xiong, X.; Keller, G.R.; Wu, X. GEO-LEO reflective band intercomparison with bidirectional reflectance distribution function and atmospheric scattering corrections. *J. Appl. Remote Sens.* **2018**, *12*, 014002-1–014002-13. [\[CrossRef\]](#)
28. Yu, F.; Wu, X.; Grotenhuis, M.; Qian, H. Inter-Calibration of GOES Imager Visible Channels over the Sonoran Desert. *J. Geophys. Res. Atmos.* **2014**, *119*, 8639–8658. [\[CrossRef\]](#)
29. Adachi, Y.; Kikuchi, R.; Matsuoka, M.; Ichii, K.; Yoshioka, H. Reflectance comparison between Himawari-8 AHI and Terra MODIS over a forest of Shikoku region. In Proceedings of the SPIE DL 10777—Land Surface and Cryosphere Remote Sensing IV, Honolulu, HI, USA, 24–26 September 2018. [\[CrossRef\]](#)
30. Myneni, R.; Knyazikhin, Y.; Park, T. MOD15A2H MODIS/Terra Leaf Area Index/FPAR 8-Day L4 Global 500m SIN Grid V006; NASA EOSDIS Land Processes Distributed Active Archive Center (LP DAAC) at the USGS Earth Resources Observation and Science (EROS) Center: Sioux Falls, South Dakota, 2018. Available online: <https://lpdaac.usgs.gov/products/mod15a2hv006/> (accessed on 18 March 2019). [\[CrossRef\]](#)
31. ALOS-2/ALOS Science Project Earth Observation Research Center (EORC) Japan Aerospace Exploration Agency (JAXA). *HLULC 30 m Resolution Map of Japan (2014–2016)(ver.18.03)*; Earth Observation Research Center, Japan Aerospace Exploration Agency: Tsukuba, Ibaraki, Japan, 2018. Available online: https://www.eorc.jaxa.jp/ALOS/en/lulc/lulc_index.htm (accessed on 18 March 2019).
32. MODIS Characterization Support Team (MCST). *MODIS 1 km Calibrated Radiances Product*; NASA MODIS Adaptive Processing System; Goddard Space Flight Center: Greenbelt, MD, USA, 2018. doi:10.5067/MODIS/MOD021KM.006. Available online: <https://modaps.modaps.eosdis.nasa.gov/services/about/products/c6/MOD021KM.html> (accessed on 18 March 2019).
33. MODIS Characterization Support Team (MCST). *MODIS Geolocation Fields Product*; NASA MODIS Adaptive Processing System; Goddard Space Flight Center: Greenbelt, MD, USA, 2018. Available online: <https://modaps.modaps.eosdis.nasa.gov/services/about/products/c6/MOD03.html> (accessed on 18 March 2019). [\[CrossRef\]](#)
34. Xiong, J.; Toller, G.; Sun, J.; Wenny, B.; Angal, A.; Barnes, W. *MODIS Level 1B Algorithm Theoretical Basis Document*; MODIS Characterization Support Team; Goddard Space Flight Center: Greenbelt, MD, USA, 2013. Available online: <https://mcst.gsfc.nasa.gov/content/11b-documents> (accessed on 18 March 2019).
35. Xiong, X.; Sun, J.Q.; Esposito, J.A.; Guenther, B.; Barnes, W.L. MODIS reflective solar bands calibration algorithm and on-orbit performance. *SPIE Opt. Remote Sens. Atmos. Clouds III* **2002**, *4891*, [\[CrossRef\]](#)
36. Ackerman, S.; et al. *MODIS Atmosphere L2 Cloud Mask Product*; NASA MODIS Adaptive Processing System; Goddard Space Flight Center: Greenbelt, MD, USA, 2018. doi:10.5067/MODIS/MOD35_L2.061. Available online: https://modaps.modaps.eosdis.nasa.gov/services/about/products/c61/MOD35_L2.html (accessed on 18 March 2019).
37. Cihlar, J.; Manak, D.; D'Iorio, M. Evaluation of compositing algorithms for AVHRR data over land. *IEEE Trans. Geosci. Remote Sens.* **1994**, *32*, 427–437. [\[CrossRef\]](#)
38. Lewis, E.E.; Miller, W.F. *Computational Methods of Neutron Transport*; Wiley: New York, NY, USA, 1984.
39. Yoshioka, H. *Applications of Transport Theory in Optical Remote Sensing of Land Surfaces*; The University of Arizona: Tucson, AZ, USA, 1999.

40. Yoshioka, H.; Miura, T.; Huete, A.R. An isoline-based translation technique of spectral vegetation index using EO-1 Hyperion data. *IEEE Trans. Geosci. Remote Sens.* **2003**, *41*, 1363–1372. [CrossRef]
41. Edwards, M. *Global Gridded Elevation and Bathymetry (ETOPO5) Digital Raster Data on a 5-Minute Geographic (lat × lon) 2160 × 4320 (Centroid-Registered) Grid*; National Oceanic and Atmospheric Administration: Boulder, CO, USA, 1989.
42. Vermote, E.; Tanré, D.; Deuzé, J.L.; Herman, M.; Morcrette, J.J.; Kotchenova, S.Y. Second Simulation of a Satellite Signal in the Solar Spectrum-Vector (6SV). 2006. Available online: <http://6s.ltdri.org/pages/manual.html> (accessed on 9 July 2018).
43. Veefkind, P. *OMI/Aura Ozone (O3) DOAS Total Column L3 1 Day 0.25 degree x 0.25 degree V3*; Goddard Earth Sciences Data and Information Services Center (GES DISC): Greenbelt, MD, USA, 2018. [CrossRef]
44. Ishida, H.; Y. Nakajima, T. Development of an unbiased cloud detection algorithm for a spaceborne multispectral imager. *J. Geophys. Res. Atmos.* **2009**, *114*, 1–16. [CrossRef]
45. Shang, H.; Chen, L.; Letu, H.; Zhao, M.; Li, S.; Bao, S. Development of a daytime cloud and haze detection algorithm for Himawari-8 satellite measurements over central and eastern China. *J. Geophys. Res. Atmos.* **2017**, *122*, 3528–3543. [CrossRef]
46. Wolfe, R.E. MODIS Geolocation. In *Earth Science Satellite Remote Sensing Vol.1: Science and Instruments*; Qu, J.J., Gao, W., Kafatos, M., Murphy, R.E., Salomonson, V.V., Eds.; Springer: Berlin, Germany, 2006; Chapter 4, pp. 50–73.
47. Matsuoka, M.; Honda, R.; Nonomura, A.; Moriya, H.; Akatsuka, S.; Yoshioka, H.; Takagi, M. A Method to Improve Geometric Accuracy of Himawari-8/AHI “Japan Area” Data. *J. Jpn. Soc. Photogramm. Remote Sens.* **2016**, *54*, 280–289. (In Japanese) [CrossRef]
48. Angal, A.; Xiong, X.; Helder, D.; Kaewmanee, M.; Leigh, L. Assessing the calibration differences in the reflective solar bands of Terra MODIS and Landsat-7 enhanced thematic mapper plus. *J. Appl. Remote Sens.* **2018**, *12*, 12–16. [CrossRef]
49. Jacquemoud, S.; Verhoef, W.; Baret, F.; Bacour, C.; Zarco-Tejada, P.J.; Asner, G.P.; François, C.; Ustin, S.L. PROSPECT+SAIL models: A review of use for vegetation characterization. *Remote Sens. Environ.* **2009**, *113*, S56–S66. [CrossRef]
50. Ulsig, L.; Nichol, C.J.; Huemmrich, K.F.; Landis, D.R.; Middleton, E.M.; Lyapustin, A.I.; Mammarella, I.; Levula, J.; Porcar-Castell, A. Detecting Inter-Annual Variations in the Phenology of Evergreen Conifers Using Long-Term MODIS Vegetation Index Time Series. *Remote Sens.* **2017**, *9*, 49. [CrossRef]
51. National Astronomical Observatory of Japan. Local Calendar. Ephemeris Computation Office NAOJ. 2018. Available online: <https://eco.mtk.nao.ac.jp/koyomi/dni/index.html.en> (accessed on 18 March 2019).



© 2019 by the authors. Licensee MDPI, Basel, Switzerland. This article is an open access article distributed under the terms and conditions of the Creative Commons Attribution (CC BY) license (<http://creativecommons.org/licenses/by/4.0/>).